JOURNAL OF GEOPHYSICAL RESEARCH, VOL. ???, XXXX, DOI:10.1002/,

Structure and Transport of the North Atlantic Current in the Eastern Subpolar Gyre from Sustained Glider Observations

L. Houpert[1], M. Inall[1], E. Dumont[1], S. Gary[1], C. Johnson[1], M. Porter[1], W. Johns[2], S.A. Cunningham[1]

[1]Scottish Association for Marine Science, Oban, UK

[2]Rosenstiel School of Marine and Atmospheric Science, Miami, US

Key Points.

- Two branches of the North Atlantic Current (named the Hatton Bank Jet and the Rockall Bank Jet) are revealed by repeated glider sections
- 6.3 ± 2.1Sv are carried by the Hatton Bank Jet in summer, about 40% of the upper-ocean transport by the North Atlantic Current at 59.5°N
- 30% of the Hatton Bank Jet transport is due to the vertical geostrophic shear while the Hatton-Rockall Basin currents are mostly barotropic

Abstract. Repeat glider sections obtained during 2014-2016, as part of the Overturning in the Subpolar North Atlantic Program (OSNAP), are used to quantify the circulation and transport of North Atlantic Current (NAC) branches over the Rockall Plateau. Using sixteen gliders sections collected along 58°N and between 21°W and 15°W, absolute geostrophic velocities are calculated and subsequently the horizontal and vertical structure of the transport are characterized. The annual mean northward transport (± standard deviation) is 5.1 ± 3.2 Sv over the Rockall Plateau. During summer (May to October), the mean northward transport is stronger and reaches 6.7 ± 2.6 Sv. This accounts for 43% of the total NAC transport of upper-ocean waters ($\sigma_O < 27.55$kg.m^{-3}) estimated by *Sarafanov et al.* [2012] along 59.5°N, between the Reykjanes Ridge and Scotland. Two quasi-permanent northward-flowing branches of the NAC are identified: (i) the Hatton Bank Jet (6.3 ± 2.1 Sv) over the eastern flank of the Iceland Basin (20.5°W to 18.5°W); and (ii) the Rockall Bank Jet (1.5 ± 0.7 Sv) over the eastern flank of the Hatton-Rockall Basin (16°W to 15°W). Transport associated with the Rockall Bank

Jet is mostly depth-independent during summer, while 30% of the Hatton Bank jet transport is due to vertical geostrophic shear.

Uncertainties are estimated for each individual glider section using a Monte Carlo approach and mean uncertainties of the absolute transport are less than 0.5 Sv. Although comparisons with altimetry-based estimates indicate similar large-scale circulation patterns, altimetry data do not resolve small mesoscale current bands in the Hatton-Rockall Basin.

1. Introduction

The Atlantic Meridional Overturning Circulation (AMOC) is characterized by a northward flux of warm upper-ocean waters and a compensating southward flux of cool deep waters, playing a fundamental role in the global climate system and its variability [*IPCC*, 2014; *Buckley and Marshall*, 2016]. Heat advected northward as part of the upper AMOC limb plays an important role in moderating western European climate [*Rhines et al.*, 2008] and is linked to the decline of Arctic sea ice [*Serreze et al.*, 2007] and mass loss from the Greenland Ice Sheet [*Straneo et al.*, 2010]. In addition, variations in AMOC strength are believed to influence North Atlantic sea surface temperatures, with potential impacts on rainfall over the African Sahel, Atlantic hurricane activity and summer climate over Europe and North America [*Zhang and Delworth*, 2006; *Sutton*, 2005; *Smith et al.*, 2010].

Subtropical waters enter the North Atlantic Subpolar Gyre (SPG) through the upper part of the North Atlantic Current (NAC, Fig. 1), strongly constrained by bathymetry [*Daniault et al.*, 2016]. About 60% (12.7 Sv) of the waters carried in the upper limb of the AMOC ($\sigma_0 < 27.55$) by the NAC and the Irminger Current are estimated to recirculate in the SPG; 10.2 Sv of this recirculating water gains density and contributes to the lower limb of the AMOC, while 2.5 Sv exits the Irminger Sea in the Western Boundary Current in the upper limb [*Sarafanov et al.*, 2012]. The remaining 40% of upper-ocean water (between 7.5 Sv and 8.5 Sv) is carried poleward by the NAC between Greenland and Scotland [*Hansen et al.*, 2010; *Rossby and Flagg*, 2012], with the majority (90%) flowing east of Iceland. Although the amounts of warm upper-ocean waters recirculating and exiting the gyre are relatively well known, the energetic eddy field [*Heywood et al.*, 1994] challenges the identification of an unequivocal relationship between the NAC branches in the eastern basin and those at the Mid-Atlantic Ridge [*Daniault et al.*, 2016].

The Rockall Plateau (RP), also known as Rockall-Hatton Plateau, is characterized by a shallow topography and is formed by the Hatton Bank (HB), the Hatton Rockall Basin (HRB) and the Rockall Bank (RB), as seen in Fig. 1 and 2a. Weak stratification leads to a small radius of deformation (<10km, [*Chelton et al.*, 1998]), this radius of deformation, a characteristic scale of the mesoscale eddy field, requires an appropriate sampling strategy to resolve and adequately characterize the flow. All previous observations from research vessels in this region have a nominal station spacing too large (about 30-50km, [*Bacon*, 1997; *Sarafanov et al.*, 2012; *Holliday et al.*, 2015]) to correctly resolve the mesoscale field over the RP.

Inaccuracies in knowledge of the geoid in this region [*Chafik et al.*, 2014] also lead to uncertainties in altimetry-derived estimates of the circulation and its variability. To resolve the net circulation over the RP, a glider endurance line was designed from the RB to a deep mooring located in the Iceland Basin at 21°W, as part of the Overturning in the Subpolar North Atlantic Program (OSNAP) [*Lozier et al.*, 2017] (Fig. 2a). OSNAP is a transatlantic observing system consisting of multiple mooring arrays supplemented by the repeat glider section across the RP.

We present data from 16 glider sections collected along 58°N, between 21°W and 15°W from July 2014 to August 2016. Glider and altimetry data are presented in section 2. In section 3, we introduce the methods used to calculate absolute geostrophic velocity from glider measurements. In Section 4, we present and discuss our results on the spatial structure of the flow and associated transport over the RP, and compare them with altimetry-based estimates. Section 5 summarizes the principal findings of this study.

2. Data

2.1. Glider sections

The gliders used in the present study perform saw-tooth trajectories from the surface to maximum depths of 1000m. With a pitch angle (of above 25°) much larger than isopycnal slopes, glider dives and climbs can be considered as quasi-vertical profiles. Using a ballast pump and wings, they achieve vertical speeds of 10-20 cm.s^{-1} and forward speeds of 20-40 cm.s^{-1}. They are designed for missions of several thousand kilometers and durations of many months, well suited to observe ocean boundary currents [*Testor et al.*, 2010; *Liblik et al.*, 2016; *Rudnick*, 2016; *Lee and Rudnick*, 2018]. Consecutive surfacings are separated by about 2-6km and 4-6h when diving to 1km depth (see Table 1, for the OSNAP mission statistics). Over each dive cycle, the depth-average current (DAC) can be derived from the Seaglider dead reckoning navigation and GPS fixes at surface. The DAC accuracy is within 1 cm.s^{-1} for a glider with stable flight characteristics [*Eriksen et al.*, 2001; *Todd et al.*, 2011]. Owing to their direct DAC measurement, gliders produce absolutely referenced geostrophic velocity that can be used to accurately quantify current transports [*Eriksen et al.*, 2001; *Rudnick and Cole*, 2011].

From July 2014 to July 2016, five gliders were deployed as part of the UK-OSNAP glider program. Sixteen sections, one section every 1-2 months, were completed over the RP (Fig. 2a). In total 6000 temperature and salinity profiles were acquired west of 15°W. To reduce energy demand, the Conductivity-Temperature-Depth (CTD) packages on Seagliders are unpumped and the cell is flushed by flow past the glider. Glider speed changes slowly, providing a nearly steady flushing rate of the conductivity cell, just as provided conventionally by a pump [*Eriksen et al.*, 2001]. Automatic quality control protocols are applied on the raw temperature/salinity data: spikes are removed; and the thermistor lag and thermal-inertia of the conductivity sensors are corrected by the Seaglider basestation v2.09 [*University of Washington*, 2016]. Suspicious data points are identified by comparing to a reference database (World Ocean Data Base [*Boyer et al.*, 2013]) and OSNAP cruise and mooring data [*Lozier et al.*, 2017]). 5.7% of salinity data and 2.2% of temperature data over RP are flagged as bad and are not used in this work.

The measurement accuracies of the CT sensors are given by the manufacturer Sea-Bird Scientific: 0.002°C for temperature and 0.005 S/m for conductivity (equivalent to an accuracy of 0.05 in salinity for standard conditions: T=15°C, S=35, P=0dbar). Point by point comparisons are made between the Seaglider CTD and calibrated SBE37 (microcat) T/S sensors on OSNAP mooring M4 at 58°N, 21°W. We kept only the glider profiles performed near the mooring (<5km). We found that the differences are lower than 0.26°C in temperature and 0.03 in salinity. However, this discrepancy in temperature cannot be considered as bias: although the temperature and salinity standard deviation in the top 1000m are the smallest at 900m, the standard deviation of the temperature time-series from the 900m-moored SBE37 (0.37°C) is two orders of magnitude larger than the measurement accuracy provided by the manufacturer. Therefore mooring data cannot be used for cross-calibration with the glider temperature measurements. The standard deviation of the salinity data at 900m depth (0.03) has the same order of magnitude as the expected accuracy for the the salinity measurement and therefore the 900m-moored SBE37 can be used to assess the accuracy of the glider salinity data. We estimate, from the glider-mooring comparisons, that the salinity measurement accuracy is consistent with the accuracy provided by the manufacturer Sea-Bird Scientific.

The glider flight model influences estimates of vertical velocities, thermal-inertia in the CT system and DAC. The internal flight model fit is improved by regressing variable buoyancy device and hydrodynamic parameters following the method used in [*Frajka-Williams et al.*, 2011], for each glider mission. Vertical velocities are derived from regressions from the difference between the predicted glider flight speed from the flight model and the observed glider vertical velocity from first difference pressure data. Applying regressions for each glider mission, the root mean square difference of the vertical velocity estimated by the Seaglider is less than 2.0 cm.s^{-1} (from 0.8 to 1.9 cm.s^{-1} depending on the particular glider mission), indicating an optimized flight model fit.

2.2. Altimetry

We use delayed time data from the SSALTO/DUACS system [*Pujol et al.*, 2016]: daily global absolute sea-surface dynamic topography, absolute geostrophic velocity and geostrophic velocity anomalies (spatial resolution of 0.25°). These are distributed through The Copernicus Marine and Environment Monitoring Service (CMEMS) (http://marine.copernicus.eu/documents/QUID/CMEMS-SL-QUID-008-032-051.pdf). This system consists of a homogeneous, inter-calibrated time series of sea-level anomaly and mean sea-level anomaly (combining data from thirteen missions). Absolute sea surface dynamic topography is the sum of sea level anomaly and a mean dynamic topography, both referenced over a twenty-year period (1993-2012). The combination of altimetric data with other datasets (e.g. in situ, gravimetric, satellites) is used to determine the geoid at a horizontal resolution of 125km and compute the mean dynamic topography (MDT-CNRS-CLS2013). Multivariate objective analysis (including wind and in situ data) is used to improve the large-scale solution, resulting in a final gridded horizontal resolution of 0.25°. The data are analysed from 01/01/2014 to 01/01/2016. We used the gridded surface geostrophic anomalies derived from the SLA gradients to calculate the Eddy Kinetic Energy (EKE). The surface EKE is calculated as one-half of the sum of the squared eddy velocity components.

3. Absolute Geostrophic Current and Transport from Gliders

From glider density sections and DAC, one can calculate the cross-track absolute geostrophic current. As in *Bosse et al.* [2015], we filter the density sections and DAC time series by using a gaussian moving average in order to filter out small-scale isopycnal oscillations mostly due to aliased sampling of high frequency internal waves (Fig. 3a,b). The full width at half maximum (18.8km, corresponding to a gaussian standard deviation of 8km) is chosen to be of the order of the deformation radius (<10km, [*Chelton et al.*, 1998]).

Following *Høydalsvik et al.* [2013], the cross-track geostrophic vertical shear is computed by integrating the thermal wind balance (Eq. 1):

$$\rho_0 f \frac{\partial \mathrm{v}_n}{\partial z} = -g \frac{\partial \rho}{\partial s} \tag{1}$$

where s is the along-section coordinate, z is the vertical coordinate, $\mathrm{v}_n(z)$ is the velocity normal to the section, f is the Coriolis parameter, g is the acceleration of gravity, ρ is the density and ρ_0 a reference density (1025 kg.m^{-3}).

By integrating Eq. 1 from the maximum depth H to the depth z we obtain Eq. 2:

$$\mathrm{v}_n(z) = \mathrm{v}_n(-H) \underbrace{-\frac{g}{\rho_0 f}\int_{-H}^{z}\frac{\partial\rho}{\partial s}dz}_{\mathrm{v_{BC}(z)}} \tag{2}$$

where $\mathrm{v}_n(-H)$ is the velocity at the maximum diving depth and $\mathrm{v}_{BC}(z)$ is the baroclinic component of the geostrophic velocity relative to depth H.

The vertically integrated Ekman current that the glider experiences during a dive can be estimated by dividing the local Ekman transport by the diving depth (always larger than the Ekman penetration depth in this area). Ekman transport is calculated every 6 hours on 0.5° longitude grid at 58°N, using ERA-Interim 10m-winds (https://www.ecmwf.int) for the 2014-2015 period in combination with a bulk formula for the wind stress, with a drag coefficient defined as in *Trenberth et al.* [1990]. Over the 2014-2015 period and from 21°W to 15°W, the 6-hourly DAC Ekman values vary from -1.7 cm.s^{-1} to 0.6 cm.s^{-1}. The mean ($\pm$ 1 standard deviation) is -0.06 cm.s^{-1} ($\pm$ 0.17 cm.s^{-1}), which is one to two orders of magnitude smaller than the observed mean DAC along the seection (V_{DAC}). Because of their small mean contribution, no Ekman corrections are applied to the DAC.

We estimate the dive-by-dive average tidal current to be of order 1 cm.s^{-1} by using a 1/12° Atlantic tidal prediction model with the Matlab toolbox Tidal Model Driver [*Egbert and Erofeeva*, 2002]. This tidal contribution is one order of magnitude less than the DAC associated with the mesoscale currents we are interested in. The mean displacement speed of the glider is 17.5km.day^{-1} (Table 1): therefore the spatial gaussian filter applied with a half maximum of 18.8km is equivalent to a temporal filter with half maximum of 1 day. The gaussian window effectively low-pass filters the data [*Todd et al.*, 2009; *Pelland et al.*, 2013; *Bosse et al.*, 2015]], thus the small tidal contribution is mostly removed by the filtering of V_{DAC}. The effectiveness of this method is confirmed by comparing to data initially low-pass filtered with a 48-hour Butterworth filter (tide removal filter). Results showed that the final datasets are identical when applying the gaussian moving average on raw data or on low-pass filtered data.

We can then consider that the vertical integral of $\mathrm{v}_n(z)$ over the depth of the dive (H) is equal to the DAC (V_{DAC}, Eq. 3):

$$V_{DAC} = \frac{1}{H}\int_{-H}^{0} \mathrm{v}_n(z)\,dz \tag{3}$$

By integrating Eq. 2 over the water column, and using Eq. 3, we obtain the velocity at the maximum diving depth $\mathrm{v}_n(-H)$ (Eq. 4). Then $\mathrm{v}_n(z)$ can then be estimated for each depth z by using Eq. 4 in Eq. 2.

$$\begin{aligned} V_{DAC} &= \mathrm{v}_n(-H) + \frac{1}{H}\int_{-H}^{0} \mathrm{v}_{\mathrm{BC}}(z)\,dz \\ \mathrm{v}_n(-H) &= \mathrm{V}_{\mathrm{DAC}} - \frac{1}{H}\int_{-H}^{0} \mathrm{v}_{\mathrm{BC}}(z)\,dz \end{aligned} \tag{4}$$

In summary, absolute geostrophic velocities are obtained by vertically integrating the thermal wind balance (Eq. 2) along the glider path from the surface to the maximum diving depth. The reference velocity at the maximum diving depth is deduced from the section-normal component of the DAC (Eq. 4).

The along-path geostrophic velocity fields are then projected onto a regular longitudinal grid along 58°N. For each glider section, all the nearby velocity profiles are binned onto a 0.05° regular longitude grid, and for each bin, we use the velocity profile with the closest f/h value compared to the f/h bin value.

Meridional absolute geostrophic transport (ϕ_{abs}, Eq. 5) is calculated by integrating absolute geostrophic velocity along the glider section, from the surface to 1000m, or to the bottom where the depth is less than 1000m.

$$\phi_{abs} = \iint\limits_{section} \mathrm{v}_n(z)dxdz \tag{5}$$

The uncertainty in transport is estimated for each section, using a Monte Carlo approach. The density field and reference velocities are perturbed to take into account uncertainties in: (i) the temperature-salinity data and (ii) the DAC estimated from the glider (see details in Appendix A). Each glider section is described by an ensemble of 100 randomly perturbed sections. ϕ_{abs} is then defined for each section as the mean of the 100 ensemble members, and the uncertainty on ϕ_{abs} is defined as 1 standard deviation between the 100 ensemble members (Table 2). The mean uncertainty of the absolute transport on the whole section (from 20.5°W to 15°W) is calculated by averaging uncertainty for all individual sections, and is equal to 0.46 Sv (Table 2).

4. Results

4.1. Zonal and Vertical Structure of the North Atlantic Current branches over the Rockall-Hatton Plateau

To define the spatial scales of the main currents we first look at the mean DAC from the repeated glider sections, shown in Fig. 2b. Three different flows can be distinguished: a northward flow extending from 20.5°W to 18.5°W (on the Eastern flank of the Iceland Basin, *Region R1*), a southward flow extending from 18.5°W to 16.0°W (on the Western flank of the HRB, *Region R2*), and a northward flow between 16.0°W 15.0°W (on the

Eastern flank of the HRB, *Region R3*).

The position and the zonal width of these three currents varies in time (Fig. 4a). We define the western and eastern limits of the northward flowing currents over Region R1, and the western limit over Region R3, as the zero-crossing locations of the meridional component of the DAC (Fig. 4a). The eastern limit of the northward flow in Region R3 is set to the easternmost point of the section, on Rockall Bank at 15°W. The horizontal extent of the southward flow in Region R2 is defined as the area between these two northward flows. The mean western and eastern limits of all individual sections are similar to those on the mean DAC time-series (Fig. 2b).

Sixteen glider sections spanned the entire region of study from 15°W to 21 °W. The mean absolute meridional geostrophic velocities are derived from all sections (Fig. 5a). Northward velocities (positive values) extend over the top 1000m of the water column in Region R1 and in Region R3. These two northward flows seem to be semi-permanent branches that form part of the total NAC flow, and are named hereafter the Hatton Bank Jet (Region R1) and the Rockall Bank Jet (Region R3). A southward flow is seen in between these two jets in Region R2.

The maximum mean northward geostrophic velocities are respectively 0.09 m.s^{-1} and 0.08 m.s^{-1} (Fig. 5a), whilst the maximum geostrophic velocities measured during the observing period are respectively 0.25 m.s^{-1} and 0.22 m.s^{-1}. The variability of the current, shown by the standard deviation between sections (Fig. 5b), is largest in the top 400m west of 18°W. This higher variability may be due to the meandering of the Hatton Bank

Jet and to the presence of two distinct cores which can be seen on the mean section as two local maxima centered on 19°W and 19.9°W (Fig. 5). Two branches appear to form upstream at the entrance of the HRB, around 55° N / 21°W: one branch enters the center of the HRB, while the other flows between Edoras Bank and HB (Fig. 2a, see also [*Xu et al.*, 2015]). To examine the vertical structure and coherency of the flow, we show in Fig. 4b the absolute geostrophic velocity near the surface and at depth. The near surface velocity (0-10m) and the velocity below the seasonal pycnocline (Fig. 4c), averaged from 500 to 1000m (or to the bottom if shallower than 1000m), have a similar time and space variability, indicating that the flow is vertically coherent but surface-intensified.

In Region R2, from 18.5°W to 16.0°W, the prevailing flow is southward (Fig. 5a) with an intensity varying in time and space (Fig. 4). The mean absolute geostrophic velocity is centered between 18°W and 17°W (Fig. 5a), with a value of -0.05 m.s^{-1} found at 770m depth, on the Western flank of the HRB, at 17.5°W. During the period of observation, the minimum geostrophic velocity recorded was -0.20 m.s^{-1} in April 2016, and localized in the surface layer (20m) at 18.2°W.

Although the flow appear to be meandering (Fig. 4), its mean position in each region seems to be associated with bathymetric features, particularly on steep slopes (Fig. 5a):

- the Rockall Bank Jet in Region R3 (15.5°W) is centered on the 1000m contour, on a steep bathymetry change associated with the eastern flank of the HRB,
- the core of the southward flow in Region R2 (17.5°W) is centered on the 800m contour, on the steep slope of the western flank of the HRB,

• the Hatton Bank Jet in Region R1 is divided into two cores, one associated with the steep western flank of the HB (19.0°W), and one centered on the 1700m isobath (19.9°W)

4.2. Meridional Absolute Geostrophic Transport

Meridional geostrophic velocity sections are integrated to provide absolute transport as a function of depth, density and longitude (Fig. 6). We choose to separate the 16 sections into two periods, distinguishing "winter" sections (November to April) when subpolar mode formation occurs, from the "summer" sections (May to October).

As a function of depth, the extrema of transport can be found in the top 200m (Fig. 6a, 6c). Two differences can be seen between the summer and the winter period:

1. The southward transport in Region R2 seems to be approximately equal to the northward transport in Region R3 during summer, with transport per depth over the whole section approximately equal to the transport in Region R1. However, during winter the transport per depth over the whole section is 1.5 to 2 Sv lower than the transport per depth in Region R1 (Fig. 6c), due to an increase in the southward transport in Region R2 and a decrease in the northward transport in Region R3 (Fig. 6a,6c).

2. The transport per depth during summer decreases with depth for Region R1 and Region R2, while during winter the transport per depth is more nearly constant from the surface to 600m, corresponding to the depth attained by the mixed layer during winter [*Lozier et al.*, 2017].

As a function of potential density, the extrema in transport are between $27.3 kg.m^{-3}$ and $27.4 kg.m^{-3}$ (Fig. 6b, 6d), corresponding to the density class of subpolar mode water over the RP [*Brambilla and Talley*, 2008]. A main difference between summer and winter is the smaller transport of density $< 27.3 kg.m^{-3}$ in all regions during winter, which can be explained by the occurrence of subpolar mode water formation: the lighter water masses at the surface are transformed into denser intermediate mode water through winter buoyancy losses.

A clear pattern appears, as a function of longitude, in the transports estimated in summer: the mean transport has two maxima, one around 20°W and the other around 15.5°W (Fig. 6e), while a mean southward transport is observed between 18.5°W and 17°W, consistent with the mean meridional geostrophic section (Fig. 5a), and the mean DAC section (Fig. 2b). During winter, there are not enough sections to be able to distinguish clearly a longitudinal structure of the mean transport. Only 4 sections were carried out west of 19°W, with only one section between January 1st and March 31st (Fig. 6f).

Transports are calculated on each section and for each geographical region (Fig. 7a). Mean transports are calculated for each region by averaging ϕ_{abs} over all available sections (Table 3). The transport across the whole glider section is calculated as the sum of the mean regional transports. Between 20.6°W and 15°W, the mean transport is 5.1 Sv (standard error of 1.0 Sv) with a standard deviation between sections of 3.2 Sv. During the summer period (May to October), outside the period of subpolar mode water formation, the mean transport between 20.6°W and 15°W is 6.7 Sv (standard error of 0.9 Sv) with a standard deviation between sections of 2.6 Sv.

In summer, the mean flows are higher and the standard deviation between the sections are smaller in the Hatton Bank Jet, the Rockall Bank Jet, and the overall section (Table 3). The mean flow associated with the three branches is: (i) 6.3 $\pm$ 2.1 Sv (Standard Error, *SE*: 0.8 Sv) northward associated with the Hatton Bank Jet (R1), (ii) 1.1 $\pm$ 1.4 Sv (SE: 0.5 Sv) southward over the western flank of the HRB (R2, 18.5°W to 16.0°W), (iii) 1.5 $\pm$ 0.7 Sv (SE: 0.2 Sv) northward associated with the Rockall Bank Jet (R3). In winter, the mean flow does not change significantly for the Rockall Bank Jet (1.5 $\pm$ 1.2 Sv, SE: 0.5 Sv), but appears 1 Sv stronger in Region R2 (-2.0 $\pm$ 1.1 Sv, SE:0.4 Sv) and 3.0 Sv weaker in the Hatton Bank Jet (3.3 $\pm$ 3.1 Sv, SE: 1.6 Sv).

The extrema range is greater in the Hatton Bank Jet (R1) compared with the other regions (Table 3). In Region R2 there is no significant difference for the minimum transport (-3.4 Sv in summer and -3.4 Sv in winter). However the maximum transport appears to be consistently negative in winter (-0.7 Sv) while positive values can be found in summer (maximum of 0.7 Sv). In the Rockall Bank Jet, the extrema range is 1 Sv smaller in summer (min: 0.1 Sv / max: 2.4 Sv) compared with winter (min: 0.2 Sv / max: 3.3 Sv), highlighting a more steady flow in summer. For the overall section, the extrema range is 4 Sv larger during winter (min: -2.0 Sv / max: 5.2 Sv) compared with summer (min: 5.3 Sv / max: 8.9 Sv).

Absolute transport ϕ_{abs} can be separated into depth independent (named hereafter "barotropic") ϕ_{bt} and baroclinic parts ϕ_{bc} (Eq. 6). Transport over the west part of the

HRB (Region R2) and in the Rockall Bank Jet is mostly barotropic during summer (mean ratio ϕ_{bc}/ϕ_{abs} of 0.1 and 0.0, Table 4), while in the Hatton Bank Jet, 30% of the absolute transport is due to the vertical geostrophic shear (Table 4).

$$\underbrace{\iint\limits_{section} \mathrm{v}_n(z)dxdz}_{\phi_{abs}} = \underbrace{\iint\limits_{section} \mathrm{v}_n(-H)dxdz}_{\phi_{bt}} + \underbrace{\iint\limits_{section} \mathrm{v}_{BC}dxdz}_{\phi_{bc}} \quad (6)$$

During winter, all three regions have a high standard error for the mean ratio ϕ_{bc}/ϕ_{abs} (from 0.22 to 1.04) and a high standard deviation between the sections (from 0.58 to 2.08). This highlights that the winter baroclinic transport has a variable contribution, compared with a more "steady" summer period. Ratios for individual sections can be lower than -1 during winter months (see *min* in Table 4), indicating a baroclinc transport similar to or larger than the barotropic transport. A possible explanation for this increase in the "baroclinicity" of the flow can be found in the winter intensification of surface buoyancy forcing. Indeed, other studies in regions of water mass formation have shown that surface buoyancy forcing can excite wintertime currents and create a baroclinic shear in the flow [*Lilly et al.*, 1999; *Howard et al.*, 2015].

5. Discussion

5.1. Comparison to altimetry

By analyzing ADCP data collected on a repeat section from Greenland to Scotland, [*Chafik et al.*, 2014] show that satellite altimetric sea surface height data are in overall good agreement with geostrophically estimated sea-level from surface ADCP velocity data. However, they found that altimetric data are unable to resolve mesoscale structures of the topographically-defined mean circulation, especially over the Banks Region shown on Fig. 1. To quantify the difference involved in using absolute surface geostrophic current from altimetry (V_{surf}^{alti}) to reference the geostrophic shear in the region of our glider study, we calculate absolute geostrophic current referenced to altimetry-derived surface absolute geostrophic current $\mathrm{v}_n^{alti}(z)$, by integrating Eq. 1 from the depth z to the surface (Eq. 7):

$$\mathrm{v}_n^{alti}(z) = \mathrm{V}_{surf}^{alti} + \frac{g}{\rho_0 f}\int_z^0 \frac{\partial \rho}{\partial s} dz \qquad (7)$$

A longitudinal section of the mean absolute meridional geostrophic velocity referenced to the surface absolute geostrophic current from satellite altimetry is shown in Fig. 5c. The differences with the mean absolute geostrophic current derived from the DAC (Fig. 5a) may be summarized as follows: 1) a decrease in the velocity in the core of the Hatton Bank Jet (at 19.8°W); 2) a stronger northward flow in the eastern part of Region R2 (17.2°W/16.1°W), leading to less overall southward transport in region R2; 3) a less intensified and broadened core of the Rockall Bank Jet (16.0°W/15.0°W), with a shift of the core from the 1000m depth contour in glider observations (Fig. 5a) to the 400m contour in altimetry-based estimate.

By using Eq. 5 on $\mathrm{v}_n^{alti}(z)$, surface absolute geostrophic currents from altimetry are used to calculate the meridional absolute geostrophic transport ϕ_{abs}^{alti}. The differences with the meridional absolute geostrophic transportestimated from glider DAC ϕ_{abs}^{gl} are shown on Fig. 7b, and are summarized in Table 5. A systematic bias can be observed in Region R2 and in the Hatton Bank Jet: the mean difference ($\pm$ 1 standard deviation) $\phi_{abs}^{alti} - \phi_{abs}^{gl}$ is equal to 2.1 ($\pm$ 1.1) Sv in Region R2 and of -1.1 ($\pm$ 1.1) Sv in the Hatton Bank Jet. This indicates an overestimation of the northward transport in the Western HRB and an underestimation of the transport of the Hatton Bank Jet fro the altimetry-based estimate. These regional biases appear to compensate each other, as on the overall section (20.5°W/15.0°W), the mean difference (± 1 standard deviation) is equal to 0.4 ± 1.3 Sv. By looking only in summer, this difference drops to 0.1 ± 0.8 Sv. The biases are not dependent on the glider mission or on the direction of the glider section (eastward or westward) suggesting that they are related to the delayed time gridded products, rather than glider observational errors.

Pujol et al. [2016] indicated that geostrophic currents estimated by satellite are underestimated compared to in situ observations; specifically they demonstrated that the gridded products are not adapted to resolve the small mesoscale. The comparison with the spectral content computed from full-resolution Saral/AltiKa 1 Hz along-track measurements shows that nearly 60 % of the energy observed in along-track measurements at wavelengths ranging from 200 to 65 km is missing in the SLA gridded products. Thus, the non-resolution of the small mesoscale current bands in the Hatton-Rockall Basin, are not resolved because of to the mapping methodology combined with altimeter constellation sampling capability.

5.2. EKE and variability of the Hatton Bank Jet

The mesoscale variability in the subpolar North Atlantic and the intensity of the eddy activity represented by the eddy kinetic energy (EKE) has been documented in several studies (e.g. [*Heywood et al.*, 1994; *White and Heywood*, 1995; *Volkov*, 2015]). At mid-latitudes away from topography, areas of high EKE appear to be associated with areas of energetic currents, therefore changes in the patterns of EKE can be indicative of changes in the strong current systems [*White and Heywood*, 1995]. Analyses of the EKE field in the subpolar North Atlantic over different periods have shown that regions of high eddy activities are mostly associated with regions of strong currents ([*Heywood et al.*, 1994; *White and Heywood*, 1995; *Reverdin et al.*, 2003; *Chafik et al.*, 2014; *Volkov*, 2015]). We computed the mean surface EKE from satellite altimetry between 2014 and 2016 (Fig. 8a) and found similar large scale patterns as the studies listed above: the highest EKE is located in the Iceland Basin (in the northward extension of the Maury Channel) and in the Rockall Trough.

The presence of cyclonic and anticyclonic eddies was observed and documented in the Iceland Basin since the 1990s [*Harris et al.*, 1997; *Martin et al.*, 1998; *Wade and Heywood*, 2001; *Read and Pollard*, 2001]. *Zhao et al.* [2018a] used high-resolution observations to document the structure of an anticyclonic eddy found during the June-November 2015 period in the Iceland Basin (58°N - 59°N / 23°W - 21°W). They also found similar anticyclonic eddies in high-resolution numerical model simulations, which they used to explore eddy formation. It appears that the main generation mechanisms are baroclinic and barotropic instabilities due to the intensification of the North Atlantic Current over the western slope of the HB. The authors indicate that the westward propagation of these eddies into the central Iceland Basin leads to a superposition of the westward NAC current branch (centred between 24°W - 23°W along 58°N, see figs. 1, 8a) onto the eddies, yielding asymmetric velocity structure. By examining 23 years of altimetry data, *Zhao et al.* [2018b] estimate that this type of anticyclonic eddy occupies this region for at least two months at a time and a new eddy is generated every few months, leading to a permanent imprint on the long-term mean ADT map, centered on 58.5°N / 22°W (Figs. 2a, 8a). The authors also found that the presence or absence of this eddy appears to make a significant contribution to the total poleward heat transport variability on time scales from sub-seasonal to interannual.

The main reason for the higher standard deviation between 21°W and 18°W (Fig. 5b) is likely to be due to the meandering of the Hatton Bank Jet associated with the strong mesoscale eddy activity identified by *Zhao et al.* [2018b]. The meridional component of the velocities associated with this anticyclonic eddy centered on 22.5°W can also be seen on the two longest glider sections in June and September 2015 (Fig. 4a), but with the northward flowing side of the eddy only partly resolved. Through the instabilities of the NAC, the generation of these anticyclonic eddies along the western slope of the HB will also impact the meridional transport in this region.

Although the west flank of the HB appears to be on average one of the main pathways of the NAC (between 21°W and 19°W, along 58°N, see fig. 1a), the eddy mesoscale activity can potentially deflect the NAC away from the HB flank towards the central Iceland Basin (Fig.8b,c). For example, in January 2015, negative transport values on the western flank of the HB (Fig. 7a) appear to be associated with a strong eddy activity from 56°N to 59°N centered on 21°W (Fig.8c), which appears to deflect the Hatton Bank Jet in the Iceland Basin. In August 2014, the NAC is crossing 58°N between 21°W and 19°W (Fig.8b), however large meanders are present above and below 58°N and the Hatton Bank Jet is deflected towards the central Iceland Basin before it reaches 59°N. One year later, in August 2015, the pathway of this NAC branch is different: it crosses 58°N between 21°W and 19°W and flows northward along the HB (Fig.8d), as in the two-year average map (Fig.8a). The deflection of the NAC away from the western flank of the HB, such as in August 2014 and January 2015, appears to be occasional as it cannot be seen in the 2-year average (Fig.8a).

5.3. Spatial structure of the North Atlantic Current branches in the Eastern Subpolar Gyre

Our transport estimates along 58°N from 21°W to 15°W are in good agreement with absolute transport estimates from the 2014 and 2016 OSNAP hydrographic cruises. *Holliday et al.* [2018] computed the absolute northward transport in the upper-layer ($\sigma_0 < 27.50 kg.m^{-3}$), between 21°W and 14°W, finding 6.4 Sv in July 2014 and 5.5 Sv in July 2016. These estimates are very close to our summer mean of 6.7 Sv, calculated in the upper 1000m, from 20.5°W to 15°W.

Sarafanov et al. [2012] and *Rossby et al.* [2017] both quantify the meridional transport across 59.5°N using different techniques. *Sarafanov et al.* [2012] combined 2002-2008 yearly hydrographic measurements with satellite altimetry data and found that 15.5 Sv is transported by the NAC between the Reykjanes Ridge and Scotland (Fig. 9), in the upper-layer ($\sigma_0 < 27.55 kg.m^{-3}$). *Rossby et al.* [2017] also found 15.5 Sv along 59.5°N but for a different time period (2012-2016) and using completely different data and a different methodology: they combined measurements of currents from the surface to 700m from a shipboard ADCP with Argo profiles.

In order to compare their estimates (extending from the Reykjanes Ridge to Scotland) with our results, we used the July 2014 and July 2016 transports computed by *Holliday et al.* [2018] and take the mean: -2.2 Sv East of the Reykjanes Ridge (-3.2 in 2014 and -1.2 in 2016), 4.3 Sv in the central Iceland (4.0 in 2014 and 4.5 in 2016). In the Rockall Trough, transport estimates were very different between the two years: 7.3 Sv in 2014 and 0.2 Sv in 2016. Therefore, we choose to take the long-term average value of 3.0 Sv computed by *Holliday et al.* [2015] from 11 complete occupations between 1997 and 2014 (northward transport in the upper 1100m relative to a level of no motion $\sigma_0 = 27.68 kg.m^{-3}$). This value is very close to the 3.7 Sv found by *Holliday et al.* [2000] from 24 complete occupations during the 1975-1998 period (northward transport above 1200m, relative to a level of no motion at 1200m). By adding the transports for these different regions along the "OSNAP section", we find a total of 11.8 Sv which is 3 Sv less than *Sarafanov et al.* [2012] and *Rossby et al.* [2017] estimates.

South of our glider section, the repeated hydrographic OVIDE section were analysed by *Daniault et al.* [2016] to compute the 2002-2012 mean summer transport across the section (Fig. 9). They identified the signature of NAC branches, which have been reported to cross the Mid-Atlantic Ridge over the Charlie-Gibbs Fracture Zone (Northern Branch), the Faraday Fracture Zone (Central Branch) and the Maxwell Fracture Zone (Southern Branch), shown on Fig. 1 (see also [*Pollard et al.*, 2004; *Bower and von Appen*, 2008]). The Northern and Central branches have been reported to head northeastward to the central Iceland Basin, the RP and the Rockall Trough [*Flatau et al.*, 2003; *Orvik and Niiler*, 2002; *Pollard et al.*, 2004; *Hakkinen and Rhines*, 2009]. Using time-averaged altimetry-derived velocities, *Daniault et al.* [2016] found that after crossing the Maxwell Fracture Zone, the Southern Branch splits into two between the Mid-Atlantic Ridge and the OVIDE section. One branch (SB1) crosses OVIDE at 48.5°N, 21.5°W and continues toward the Rockall Trough and the RP, while the other branch (SB2) crosses OVIDE at 46.1°N, 19.4°W and veers southward in the West European Basin (Figs. 1, 9). The sum of the 2002-2012 mean OVIDE transport in the upper-layer ($\sigma_1 < 32.15 kg.m^{-3}$) for the East Reykjanes

Ridge Current (-4.1 Sv), the Northern Branch (3.3 Sv), the Central Branch (8.1 Sv), and Southern Branch SB1 (8.1 Sv) is 15.4 Sv. Remarkably, this number is consistent with the 15.5 Sv calculated by *Sarafanov et al.* [2012] and *Rossby et al.* [2017] who computed the transport in the upper-layer ($\sigma_0 < 27.55 kg.m^{-3}$) along 59.5°N, from the Reykjanes Ridge to Scotland (2002-2008 summer mean in *Sarafanov et al.* [2012], 2012-2016 mean in *Rossby et al.* [2017]).

This good agreement with the 2012-2016 mean calculated by *Rossby et al.* [2017] led us to formulate the hypothesis that the 2002-2012 summer mean transport calculated across the OVIDE section can also be representative of the 2014-2016 summer mean. Therefore, we then can discuss the NAC transport across the OVIDE section with respect to our results at 58°N. We also computed the mean Absolute Dynamic Topography (ADT) contours over the 2014-2016 period. The -0.2 m and 0 m ADT contours appear to delimit the SB1 branch on the OVIDE section (Fig. 9). These contours cross 58°N at 19.5°W and 8°W, suggesting that the 8.1 Sv from the SB1 branch could feed the Rockall Trough and most of the RP, as already discussed by *Daniault et al.* [2016]. The -0.3 m and -0.2 m ADT contours delimit the Central Branch on the OVIDE section, feeding the eastern Iceland Basin (23.5°W to 19.5°W). The 6.3 Sv associated with the Hatton Bank Jet (between 21°W and 18.5°W) is supplied by both the Central Branch and the Southern Branch SB1. Interestingly, the horizontal structure of the Hatton Bank Jet meridional velocity presents two cores/branches: one centered on 20°W and another on 19°W (Fig. 5a). These two branches are delimited by the -0.2 m ADT contour (crossing the glider section at 19.5°W) which also delimits the Central Branch and the Southern Branch SB1 on the OVIDE section.

By adding the mean upper-layer transports computed by *Holliday et al.* [2018] between 31°W and 21°W with the 2014-2016 mean summer transport from this study, we find an upper-layer transport of 8.8 Sv between 31°W and 15°W. Across OVIDE, the sum of the East Reykjanes Ridge Current with the Northern Branch and the Central Branch correspond to a upper-layer transport of 7.3 Sv toward the Iceland Basin and RP. Therefore the Southern branch SB1 (8.1 Sv) would have to provide the additional 1.5 Sv over the RP. The ADT contours (Fig. 9) suggest that the remaining 6.6 Sv would feed the Rockall Trough. Although this estimate is more than twice the mean transport reported previously in the Rockall Trough, it falls within the range of observed transports [*Holliday et al.*, 2000, 2015, 2018] so it is a possible avenue for closing the meridional upper-ocean transport between the Reykjanes Ridge and Scotland along 58N. In addition, *Sarafanov et al.* [2012] found a mean northward transport of 8.5 Sv between 17.5°W and 10°W, with a horizontal structure clearly indicating that most of the northward transport on this section occurs between 15°W and 12°W with the maximum centered on 13°W, in the northward extension of the Rockall Trough. Because our results indicate almost no net transport in the Hatton-Rockall Basin, most of the transport crossing the 59.5°N section between 17.5°W and 6°W has to come from the Rockall Trough. If about 2 Sv exit the Rockall Trough into the Faroe Bank Chanel [*Berx et al.*, 2013], the remaining 4 Sv will have to exit the Rockall Trough toward the Iceland Basin and therefore contribute to about 50% of the 8.5 Sv computed by *Sarafanov et al.* [2012] between 17.5°W and 10°W.

6. Conclusion

From July 2014 to August 2016, 16 UK-OSNAP glider sections were undertaken over the RP, along 58°N from 21°W to 15°W. The mean absolute geostrophic transport referenced to glider DAC $\pm$ standard deviation is 6.7 $\pm$ 2.6 Sv in summer (May to October), with three main branches (Fig. 9): (i) the Hatton Bank Jet, a northward flow of 6.3 $\pm$ 2.1 Sv along the western flank of the Hatton Bank (20.5°W to 18.5°W); (ii) a southward flow of 1.1 $\pm$ 1.4 Sv along the western flank of the Hatton-Rockall Basin (18.5°W to 16.0°W); (iii) the Rockall Bank Jet, a northward flow of 1.5 $\pm$ 0.7 Sv along the eastern flank of the Hatton-Rockall Basin (16°W to 15°W). On average, these three branches are bathymetrically steered, particularly on the steep slopes of the Hatton and Rockall Banks. The net meridional transport in summer accounts for 43% of the total NAC transport of upper-ocean waters ($\sigma_O < 27.55$) estimated by *Sarafanov et al.* [2012] and *Rossby et al.* [2017] along 59.5°N, between the Reykjanes Ridge and Scotland.

With the NAC branches in the Central Iceland Basin and in the Rockall Trough, the Hatton Bank Jet is one of the main NAC pathway in the Eastern Subpolar Gyre. The Hatton Bank Jet appears to be quasi-permanent as it can be seen on both mean absolute surface geostrophic currents from altimetry data and on mean absolute geostrophic sections from repeated glider observations along 58°N. However, it can be occasionally deflected towards the Iceland Basin due to strong mesoscale eddy activity west of the Hatton Bank.

The transport on the western and eastern parts of the Hatton-Rockall Basin is mostly independent of depth during summer, while 30% of the Hatton Bank Jet transport is baroclinic. During winter, transports have a higher variability and geostrophic currents are more baroclinic. The winter intensification of surface buoyancy forcing could be the reason for an enhanced baroclinic shear and winter subpolar mode formation, which may lead to an increase of current variability in the subpolar gyre. More glider sections in winter are needed if one wants to fully characterize and quantify the excitation of wintertime currents by surface buoyancy forcing. Fewer winter observations are available due to logistical difficulties and poor weather conditions, leading to a higher uncertainty on the mean winter meridional transport. However, additional observing efforts are being made to ensure a permanent monitoring of the Hatton Bank Jet in winter.

Comparisons with altimetry-based estimates indicate similar large-scale circulation patterns, however altimetry data are unable to resolve the small mesoscale current bands in the Hatton-Rockall Basin, which appear to be due to the mapping methodology combined with altimeter constellation sampling capability.

Appendix A: Uncertainty of the transport estimates

We used a Monte Carlo approach to assess the uncertainty of transports through individual glider sections. Uncertainties can be due to two components of the geostrophic velocity calculation: the density field and the cross-section component of the DAC. Density is derived from the measurements of conductivity and temperature of the CT sensor manufactured by Sea-bird Scientific and the primary source of uncertainty with this measurement is the drift of the sensor over the course of the glider mission. For each glider section, we create an ensemble of 100 sections of randomly perturbed densities. We add to the original density field a density drift taken from a random uniform distribution for which the boundaries ($\pm$ 0.0025 kg.m^{-3}/month) are determined from the typical stability of the CT sensors ($<$ to 0.001 $^\circ$ C/month in temperature and 0.003/month in salinity, according to Sea-Bird Scientific).

Two main sources of uncertainty can influence the DAC calculation: the accuracy of the surface GPS fixes and the compass calibration. The compass has an accuracy of 1 $^\circ$

according to the manufacturer but magnetic perturbation can invalidate a pre-deployment calibration of the compass. To tackle this problem, the Seaglider Fabrication Center developed an in-flight compass calibration, corresponding to a two-dive sequence with two different roll and pitch angles, that allows a compass calibration with in an accuracy a few degrees [*GROOM*, 2014]. In addition, for four of the five glider deployments, the compass calibration was checked on land [*GROOM*, 2014], before or after the glider mission. Most of time, the deployment or the recovery of the glider is made from a small coastal boat (where no magnetic disturbance is likely to occur between the on-land compass check and the glider mission). The rest of the time, the glider travels by sea-freight and carrier before it is possible to perform an on-land compass check. Thus, we chose the heading errors given by the on-land compass check as being representative of the heading errors of the glider during each mission. The summary of the heading-dependent errors for the different OSNAP missions is shown in Table 6.

The terms Err_{port} and Err_{stbd} indicate the heading error from compass checks made with different orientations of the glider (turned on port and starboard). For OSNAP3 and OSNAP4, the compass checks for different orientations of the glider were not possible. An Err_{min} and Err_{max} variable is defined for OSNAP3 by using the single-orientation compass check and by adding the maximal difference recorded between a compass check with a starboard orientation and a port orientation (8°). No on-land compass check was available for the OSNAP4 glider mission due to the loss of the glider at the end of the mission. However an in-flight compass calibration was performed at the beginning of the mission, thus we determined the heading error as the maximum post-mission heading error recorded for a glider which performed an in-flight compass calibration (6°).

For each dive, we produced 100 values of heading errors, taken from a random uniform distribution where the boundaries are determined by the on-land compass checks carried out pre- or post- deployment (variables Err_{port} / Err_{stbd} , Err_{min} / Err_{max} in Table 6). In addition, we produce for each glider section an ensemble of 100 perturbed start-dive GPS position and end-dive GPS position. We add to the original GPS positions an error taken from a random exponential distribution, where 95% of the distribution is in a 100m range (exponential rate of 0.0461) [Bennett and Stahr, pers. comm., 2014]. For each dive cycle, a perturbed glider heading is created by taking the mean heading of the glider during the dive (calculated from the end-dive dead reckoning position), and by adding to it the random heading error (constant for each glider mission). Then, for each dive, the perturbed start-dive GPS position and the perturbed glider heading are used to recalculate end-dive dead reckoning positions. An ensemble of 100 DAC values is obtained for each dive by calculating the distance between perturbed end-dive dead reckoning position and perturbed end-dive surface GPS position and dividing by the time of the glider dive cycle.

Then these sections of perturbed reference velocities and perturbed densities are used to calculate an ensemble of absolute geostrophic velocities and transport. For each section, our transport estimate corresponds to the mean of the 100 ensemble members and the uncertainty bars are defined as $\pm$ 1 standard deviation between the 100 ensemble members (Fig. 7a). Uncertainties calculated for each section are listed in Table 2.

Acknowledgments.

We would like to acknowledge the efforts of Karen Wilson and Colin Griffiths in piloting the gliders; and assistance recovering gliders from the officers and crew of the

R/V Pelagia and RRS Discovery. UK-OSNAP gliders, SAC, MA and LH are supported by the OSNAP NERC Large Grant (NE/K010700/1). MP is supported by the FAST-NEt NERC Consortium grant (NE/I030224/1). CJ received funding from the European Unions Horizon 2020 research and innovation programme under Grant Agreement no. 678760 (ATLAS). SAC was supported by the Blue-Action project (European Union's Horizon 2020 research and innovation programme, grant number: 727852). SFG was supported by NERC National Capability funding (R8-H12-85). This study has been conducted using E.U. Copernicus Marine Service Information. This output reflects only the authors view and the European Union cannot be held responsible for any use that may be made of the information contained therein. BODC curates the near-real time dataset (https://doi.org/10.5285/630bd9f3-2aec-2135-e053-6c86abc01eed). Please see text and references for other data sources. The authors would like to thank Jim Bennett and Dr. Fritz Stahr for their support.

References

Bacon, S. (1997), Circulation and Fluxes in the North Atlantic between Greenland and Ireland, *J. Phys. Oceanogr.*, *27*(7), 1420–1435, doi:10.1175/1520-0485(1997)027¡1420:CAFITN¿2.0.CO;2.

Berx, B., B. Hansen, S. Østerhus, K. M. Larsen, T. Sherwin, and K. Jochumsen (2013), Combining in situ measurements and altimetry to estimate volume, heat and salt transport variability through the Faroe-Shetland Channel, *Ocean Sci.*, *9*(4), 639–654, doi: 10.5194/os-9-639-2013.

Bosse, A., P. Testor, L. Mortier, L. Prieur, V. Taillandier, F. D'Ortenzio, and L. Coppola (2015), Spreading of Levantine Intermediate Waters by submesoscale coherent vortices in the northwestern Mediterranean Sea as observed with gliders, *J. Geophys. Res. Ocean.*, *120*(3), 1599–1622, doi:10.1002/2014JC010263.

Bower, A. S., and W.-J. von Appen (2008), Interannual Variability in the Pathways of the North Atlantic Current over the Mid-Atlantic Ridge and the Impact of Topography, *J. Phys. Oceanogr.*, *38*(1), 104–120, doi:10.1175/2007JPO3686.1.

Boyer, T. P., J. I. Antonov, O. K. Baranova, C. Coleman, H. E. Garcia, A. Grodsky, D. R. Johnson, R. A. Locarnini, A. V. Mishonov, T. D. O. Brien, C. R. Paver, J. R. Reagan, D. Seidov, I. V. Smolyar, M. M. Zweng, and K. D. Sullivan (2013), World Ocean Database 2013, *Sydney Levitus, Ed.; Alexey Mishonoc, Tech. Ed.*, *NOAA Atlas*(72), 209 pp, doi:http://doi.org/10.7289/V5NZ85MT.

Brambilla, E., and L. D. Talley (2008), Subpolar mode water in the northeastern Atlantic: 1. Averaged properties and mean circulation, *J. Geophys. Res. Ocean.*, *113*(4), 1–18, doi:10.1029/2006JC004062.

Buckley, M. W., and J. Marshall (2016), Observations, inferences, and mechanisms of the Atlantic Meridional Overturning Circulation: A review, *Rev. Geophys.*, *54*(1), 5–63, doi:10.1002/2015RG000493.

Chafik, L., T. Rossby, and C. Schrum (2014), On the spatial structure and temporal variability of poleward transport between Scotland and Greenland, *J. Geophys. Res. Ocean.*, *119*(2), 824–841, doi:10.1002/2013JC009287.

Chelton, D. B., R. A. DeSzoeke, M. G. Schlax, K. El Naggar, and N. Siwertz (1998), Geographical Variability of the First Baroclinic Rossby Radius of Deformation, *J. Phys.*

Oceanogr., *28*(3), 433–460, doi:10.1175/1520-0485(1998)028¡0433:GVOTFB¿2.0.CO;2.

Daniault, N., H. Mercier, P. Lherminier, A. Sarafanov, A. Falina, P. Zunino, F. F. Pérez, A. F. Ríos, B. Ferron, T. Huck, V. Thierry, and S. Gladyshev (2016), The northern North Atlantic Ocean mean circulation in the early 21st century, *Prog. Oceanogr.*, *146*(July), 142–158, doi:10.1016/j.pocean.2016.06.007.

Egbert, G. D., and S. Y. Erofeeva (2002), Efficient Inverse Modeling of Barotropic Ocean Tides, *J. Atmos. Ocean. Technol.*, *19*(2), 183–204, doi:10.1175/1520-0426(2002)019¡0183:EIMOBO¿2.0.CO;2.

Eriksen, C., T. Osse, R. Light, T. Wen, T. Lehman, P. Sabin, J. Ballard, and A. Chiodi (2001), Seaglider: a long-range autonomous underwater vehicle for oceanographic research, *IEEE J. Ocean. Eng.*, *26*(4), 424–436, doi:10.1109/48.972073.

Flatau, M. K., L. Talley, and P. P. Niiler (2003), The North Atlantic Oscillation, surface current velocities, and SST changes in the subpolar North Atlantic, *J. Clim.*, *16*(14), 2355–2369, doi:10.1175/2787.1.

Frajka-Williams, E., C. C. Eriksen, P. B. Rhines, and R. R. Harcourt (2011), Determining Vertical Water Velocities from Seaglider, *J. Atmos. Ocean. Technol.*, *28*(12), 1641–1656, doi:10.1175/2011JTECHO830.1.

GROOM (2014), Deliverable 5.3. Report describing Best practices for glider missions and sensor use: preparation, operation, calibration, intercalibration/comparison, and recovery., *Tech. rep.*, European Union - 7th Framework Programme.

Hakkinen, S., and P. B. Rhines (2009), Shifting surface currents in the northern North Atlantic Ocean, *J. Geophys. Res. Ocean.*, *114*(4), 1–12, doi:10.1029/2008JC004883.

Hansen, B., H. Hátún, R. Kristiansen, S. M. Olsen, and S. Østerhus (2010), Stability and forcing of the Iceland-Faroe inflow of water, heat, and salt to the Arctic, *Ocean Sci.*, *6*(4), 1013–1026, doi:10.5194/os-6-1013-2010.

Harris, R. P., P. Boyd, D. S. Harbour, R. N. Head, R. D. Pingree, and A. J. Pomroy (1997), Physical, chemical and biological features of a cyclonic eddy in the region of 61.10 N and 19.50 W in the North Atlantic, *Deep Sea Res. I*, *44*(11), 1815–1839.

Heywood, K. J., E. L. McDonagh, and M. A. White (1994), Eddy kinetic energy of the North Atlantic subpolar gyre from satellite altimetry, *J. Geophys. Res.*, *99*(C11), 22,525, doi:10.1029/94JC01740.

Holliday, N., R. T. Pollard, J. F. Read, and H. Leach (2000), Water mass properties and fluxes in the Rockall Trough, 19751998, *Deep Sea Res. Part I Oceanogr. Res. Pap.*, *47*(7), 1303–1332, doi:10.1016/S0967-0637(99)00109-0.

Holliday, N. P., S. A. Cunningham, C. Johnson, S. F. Gary, C. Griffiths, J. F. Read, and T. Sherwin (2015), Multidecadal variability of potential temperature, salinity, and transport in the eastern subpolar North Atlantic, *J. Geophys. Res. Ocean.*, *120*(9), 5945–5967, doi:10.1002/2015JC010762.

Holliday, N. P., S. Bacon, S. Cunningham, S. F. Gary, J. Karstensen, B. A. King, F. Li, and E. L. McDonagh (2018), Subpolar North Atlantic overturning and gyre-scale circulation in the summers of 2014 and 2016, *J. Geophys. Res. Ocean.*, (in revision).

Howard, E., A. McC. Hogg, S. Waterman, D. P. Marshall, E. Howard, A. M. Hogg, S. Waterman, and D. P. Marshall (2015), The Injection of Zonal Momentum by Buoyancy Forcing in a Southern Ocean Model, *J. Phys. Oceanogr.*, *45*(1), 259–271, doi: 10.1175/JPO-D-14-0098.1.

Høydalsvik, F., C. Mauritzen, K. Orvik, J. LaCasce, C. Lee, and J. Gobat (2013), Transport estimates of the Western Branch of the Norwegian Atlantic Current from glider surveys, *Deep Sea Res. Part I Oceanogr. Res. Pap.*, *79*, 86–95, doi: 10.1016/j.dsr.2013.05.005.

IPCC (2014), *Climate Change 2013 - The Physical Science Basis*, 1–6 pp., Cambridge University Press, Cambridge, doi:10.1017/CBO9781107415324.

Lee, C. M., and D. L. Rudnick (2018), Underwater Gliders, in *Obs. Ocean. Real Time*, edited by R. Venkatesan, A. Tandon, E. D'Asaro, and M. A. Atmanand, Springer Oceanography, pp. 123–139, Springer International Publishing, Cham, doi:10.1007/978-3-319-66493-4.

Liblik, T., J. Karstensen, P. Testor, P. Alenius, D. Hayes, S. Ruiz, K. Heywood, S. Pouliquen, L. Mortier, and E. Mauri (2016), Potential for an underwater glider component as part of the Global Ocean Observing System, *Methods Oceanogr.*, *17*, 50–82, doi:10.1016/j.mio.2016.05.001.

Lilly, J. M., P. B. Rhines, M. Visbeck, R. Davis, J. R. N. Lazier, F. Schott, and D. Farmer (1999), Observing Deep Convection in the Labrador Sea during Winter 1994/95, *J. Phys. Oceanogr.*, *29*(8), 2065–2098, doi:10.1175/1520-0485(1999)029¡2065:ODCITL¿2.0.CO;2.

Lozier, M. S., S. Bacon, A. S. Bower, S. A. Cunningham, M. Femke de Jong, L. de Steur, B. DeYoung, J. Fischer, S. F. Gary, B. J. W. Greenan, P. Heimbach, N. P. Holliday, L. Houpert, M. E. Inall, W. E. Johns, H. L. Johnson, J. Karstensen, F. Li, X. Lin, N. Mackay, D. P. Marshall, H. Mercier, P. G. Myers, R. S. Pickart, H. R. Pillar, F. Straneo, V. Thierry, R. A. Weller, R. G. Williams, C. Wilson, J. Yang, J. Zhao, and J. D. Zika (2017), Overturning in the Subpolar North Atlantic Program: A New International Ocean Observing System, *Bull. Am. Meteorol. Soc.*, *98*(4), 737–752, doi: 10.1175/BAMS-D-16-0057.1.

Martin, A. P., I. P. Wade, K. J. Richards, and K. J. Heywood (1998), The PRIME Eddy, *J. Mar. Res.*, *56*(2), 439–462, doi:10.1357/002224098321822375.

Orvik, K. A., and P. Niiler (2002), Major pathways of Atlantic water in the northern North Atlantic and Nordic Seas toward Arctic, *Geophys. Res. Lett.*, *29*(19), 2–1–2–4, doi:10.1029/2002GL015002.

Pelland, N. a., C. C. Eriksen, and C. M. Lee (2013), Subthermocline Eddies over the Washington Continental Slope as Observed by Seagliders, 200309, *J. Phys. Oceanogr.*, *43*(10), 2025–2053, doi:10.1175/JPO-D-12-086.1.

Pollard, R. T., J. F. Read, N. P. Holliday, and H. Leach (2004), Water masses and circulation pathways through the Iceland basin during Vivaldi 1996, *J. Geophys. Res. C Ocean.*, *109*(4), 1–10, doi:10.1029/2003JC002067.

Pujol, M. I., Y. Faugère, G. Taburet, S. Dupuy, C. Pelloquin, M. Ablain, and N. Picot (2016), DUACS DT2014: The new multi-mission altimeter data set reprocessed over 20 years, *Ocean Sci.*, *12*(5), 1067–1090, doi:10.5194/os-12-1067-2016.

Read, J. F., and R. T. Pollard (2001), A long-lived eddy in the Iceland Basin 1998, *J. Geophys. Res.*, *106*(C6), 11,411, doi:10.1029/2000JC000492.

Reverdin, G., P. P. Niiler, and H. Valdimarsson (2003), North Atlantic Ocean surface currents, *J. Geophys. Res. Ocean.*, *108*(C1), 2–21, doi:10.1029/2001JC001020.

Rhines, P., S. Häkkinen, and S. A. Josey (2008), *ArcticSubarctic Ocean Fluxes*, 87–109 pp., Springer Netherlands, Dordrecht, doi:10.1007/978-1-4020-6774-7.

Rossby, T., and C. N. Flagg (2012), Direct measurement of volume flux in the Faroe-Shetland Channel and over the Iceland-Faroe Ridge, *Geophys. Res. Lett.*, *39*(7), n/a–n/a, doi:10.1029/2012GL051269.

Rossby, T., G. Reverdin, L. Chafik, and H. Søiland (2017), A direct estimate of poleward volume, heat, and freshwater fluxes at 59.5N between Greenland and Scotland, *J. Geophys. Res. Ocean.*, *122*(7), 5870–5887, doi:10.1002/2017JC012835.

Rudnick, D. L. (2016), Ocean Research Enabled by Underwater Gliders, *Ann. Rev. Mar. Sci.*, *8*(1), 519–541, doi:10.1146/annurev-marine-122414-033913.

Rudnick, D. L., and S. T. Cole (2011), On sampling the ocean using underwater gliders, *J. Geophys. Res.*, *116*(C8), C08,010, doi:10.1029/2010JC006849.

Sarafanov, A., A. Falina, H. Mercier, A. Sokov, P. Lherminier, C. Gourcuff, S. Gladyshev, F. Gaillard, and N. Daniault (2012), Mean full-depth summer circulation and transports at the northern periphery of the Atlantic Ocean in the 2000s, *J. Geophys. Res. Ocean.*, *117*(1), n/a–n/a, doi:10.1029/2011JC007572.

Serreze, M. C., M. M. Holland, and J. Stroeve (2007), Perspectives on the Arctic's shrinking sea-ice cover., *Science*, *315*(5818), 1533–6, doi:10.1126/science.1139426.

Smith, D. M., R. Eade, N. J. Dunstone, D. Fereday, J. M. Murphy, H. Pohlmann, and A. A. Scaife (2010), Skilful multi-year predictions of Atlantic hurricane frequency, *Nat. Geosci.*, *3*(12), 846–849, doi:10.1038/ngeo1004.

Straneo, F., G. S. Hamilton, D. A. Sutherland, L. a. Stearns, F. Davidson, M. O. Hammill, G. B. Stenson, and A. Rosing-Asvid (2010), Rapid circulation of warm subtropical waters in a major glacial fjord in East Greenland, *Nat. Geosci.*, *3*(3), 182–186, doi:10.1038/ngeo764.

Sutton, R. T. (2005), Atlantic Ocean Forcing of North American and European Summer Climate, *Science (80-.).*, *309*(5731), 115–118, doi:10.1126/science.1109496.

Testor, P., G. Meyers, C. Pattiaratchi, R. Bachmayer, D. Hayes, S. Pouliquen, L. P. de la Villeon, T. Carval, A. Ganachaud, L. Gourdeau, L. Mortier, H. Claustre, V. Taillandier, P. Lherminier, T. Terre, M. Visbeck, J. Karstensen, G. Krahmann, A. Alvarez, M. Rixen, P.-M. Poulain, S. Osterhus, J. Tintore, S. Ruiz, B. Garau, D. Smeed, G. Griffiths, L. Merckelbach, T. Sherwin, C. Schmid, J. A. Barth, O. Schofield, S. Glenn, J. Kohut, M. J. Perry, C. Eriksen, U. Send, R. Davis, D. Rudnick, J. Sherman, C. Jones, D. Webb, C. Lee, B. Owens, R. Bachmeyer, D. Hayes, S. Pouliquen, L. Petit de la Villeon, T. Carval, A. Ganachaud, L. Gourdeau, L. Mortier, H. Claustre, V. Taillandier, P. Lherminier, T. Terre, M. Visbeck, J. Karstensen, G. Krahmann, A. Alvarez, M. Rixen, P.-M. Poulain, S. Osterhus, J. Tintore, S. Ruiz, B. Garau, D. Smeed, G. Griffiths, L. Merckelbach, T. Sherwin, C. Schmid, J. A. Barth, O. Schofield, S. Glenn, J. Kohut, M. J. Perry, C. Eriksen, U. Send, R. Davis, D. Rudnick, J. Sherman, C. Jones, D. Webb, C. Lee, and B. Owens (2010), Gliders as a Component of Future Observing Systems, in *Proc. "OceanObs'09 Sustain. Ocean Obs. Inf. Soc.*, *ESA Publication*, vol. 2, edited by J. Hall, D. E. Harrison, and D. Stammer, pp. 961–978, OceanObs'09, Venice, Italy, doi:10.5270/OceanObs09.cwp.89.

Todd, R. E., D. L. Rudnick, and R. E. Davis (2009), Monitoring the greater San Pedro Bay region using autonomous underwater gliders during fall of 2006, *J. Geophys. Res.*, *114*(C6), C06,001, doi:10.1029/2008JC005086.

Todd, R. E., D. L. Rudnick, M. R. Mazloff, R. E. Davis, and B. D. Cornuelle (2011), Poleward flows in the southern California Current System: Glider observations and numerical simulation, *J. Geophys. Res. Ocean.*, *116*(2), 1–16, doi:10.1029/2010JC006536.

Trenberth, K. E., W. G. Large, and J. G. Olson (1990), The Mean Annual Cycle in Global Ocean Wind Stress, *J. Phys. Oceanogr.*, *20*(11), 1742–1760, doi:10.1175/1520-0485(1990)020¡1742:TMACIG¿2.0.CO;2.

University of Washington (2016), Seaglider quality control manual for basestation 2.09, *Tech. rep.*, School of Oceanography and Applied Physics Laboratory, University of Washington.

Volkov, D. L. (2015), Eddy field and its spatial and temporal variability in the North Atlantic Ocean as observed with satellite altimetry Interannual Variability of the Altimetry-Derived Eddy Field and Surface Circulation in, (April 2003).

Wade, I. P., and K. J. Heywood (2001), Tracking the PRIME eddy using satellite altimetry, *Deep Sea Res. Part II Top. Stud. Oceanogr.*, *48*(4-5), 725–737, doi:10.1016/S0967-0645(00)00094-1.

White, M. A., and K. J. Heywood (1995), Seasonal and interannual changes in the North Atlantic subpolar gyre from Geosat and TOPEX/POSEIDON altimetry, *J. Geophys. Res.*, *100*(C12), 24,931, doi:10.1029/95JC02123.

Xu, W., P. I. Miller, G. D. Quartly, and R. D. Pingree (2015), Seasonality and interannual variability of the European Slope Current from 20years of altimeter data compared with in situ measurements, *Remote Sens. Environ.*, *162*, 196–207, doi:10.1016/j.rse.2015.02.008.

Zhang, R., and T. L. Delworth (2006), Impact of Atlantic multidecadal oscillations on India/Sahel rainfall and Atlantic hurricanes, *Geophys. Res. Lett.*, *33*(17), L17,712, doi:10.1029/2006GL026267.

Zhao, J., A. S. Bower, J. Yang, Lin X, and Zhou C (2018a), Structure and Formation of Anticyclonic Eddies in the Iceland Basin, *J. Geophys. Res. Ocean.*, (in revision).

Zhao, J., A. Bower, J. Yang, and X. Lin (2018b), Meridional heat transport variability induced by mesoscale processes in the subpolar North Atlantic, *Nat. Commun.*, *9*(1), 1–9, doi:10.1038/s41467-018-03134-x.

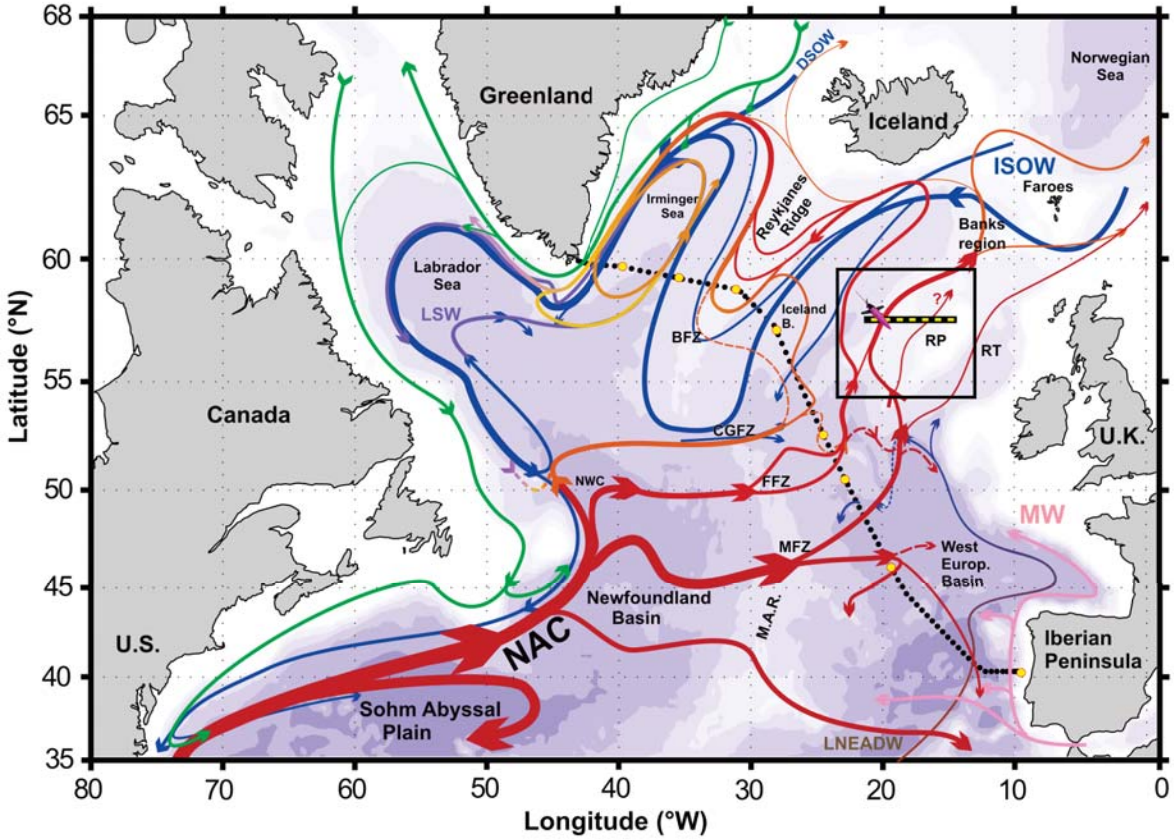

Figure 1. Schematic view of the main circulation pathways in the Subpolar North Atlantic Gyre adapted from *Daniault et al.* [2016], showing the relatively warm surface and intermediate water and the cold deep waters. The nominal UK-OSNAP glider section is shown as a yellow dashed line (from 21°W to 15°W). Absolute geostrophic and bathymetry details in the box area are shown on figure 2. Acronyms: North Atlantic Current (NAC); Deep Western Boundary Current (DWBC); Bigth Fracture Zone (BFZ); Charlie-Gibbs Fracture Zone (CGFZ); Faraday Fracture Zone (FFZ); Maxwell Fracture Zone (MFZ); Mid-Atlantic Ridge (MAR); Rockall Plateau (RP); Rockall Trough (RT);Iceland-Scotland Overflow Water (ISOW); Denmark Strait Overflow Water (DSOW); Mediterranean Water (MW); Lower Northeast Atlantic Deep Water (LNEADW); Labrador Sea Water (LSW)

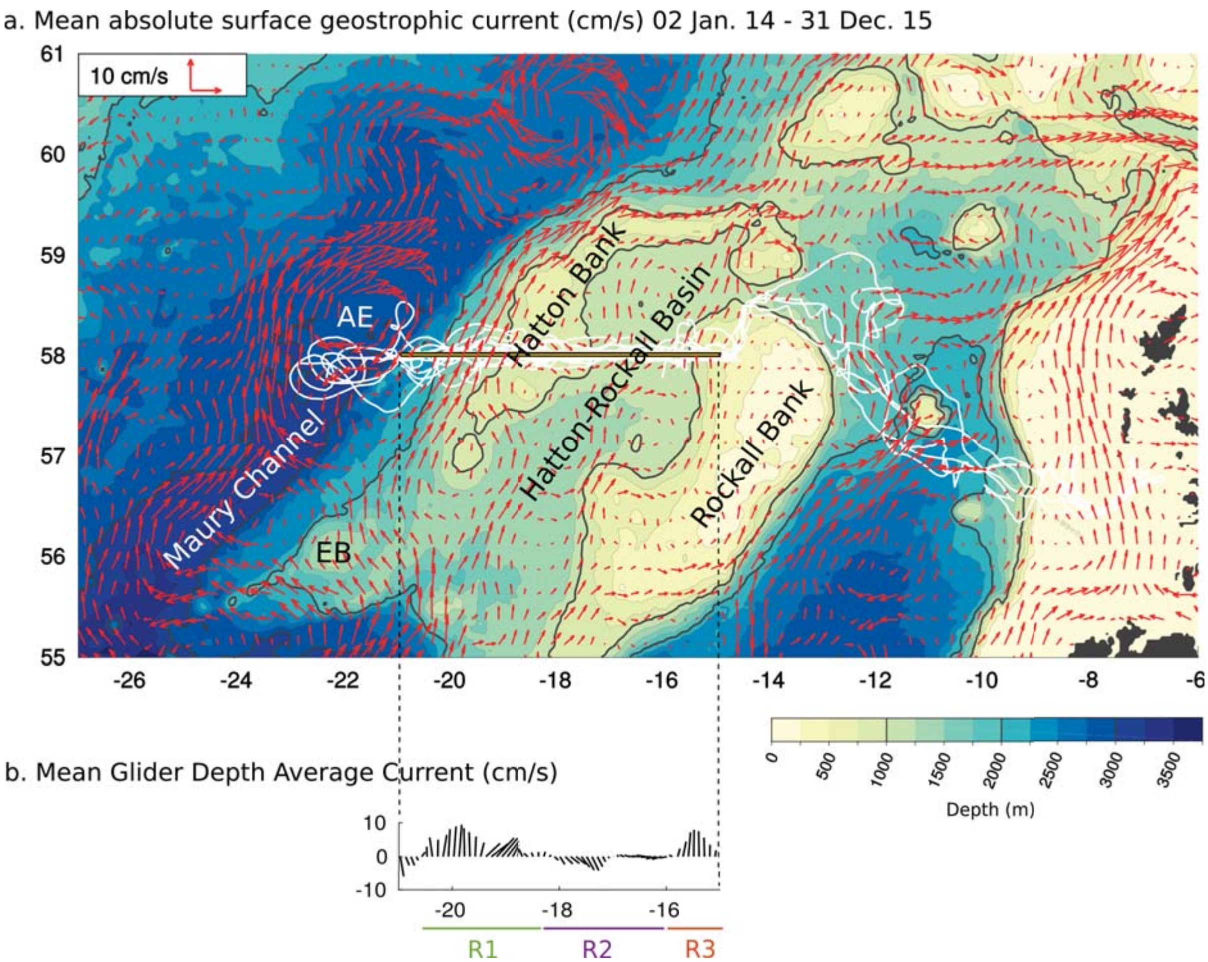

Figure 2. a) Two year mean surface absolute geostrophic current (arrows) for the 2014-2015 period, with the glider mission tracks (white) and bathymetry contours in color from GEBCO bathymetry (http://www.gebco.net/). Acronyms: Anticyclonic Eddy (AE); Edoras Bank (EB). b) Mean glider depth average current (m.s^{-1}) from 21°W to 14.5°W, with the limits of the three regions mentioned in the manuscript.

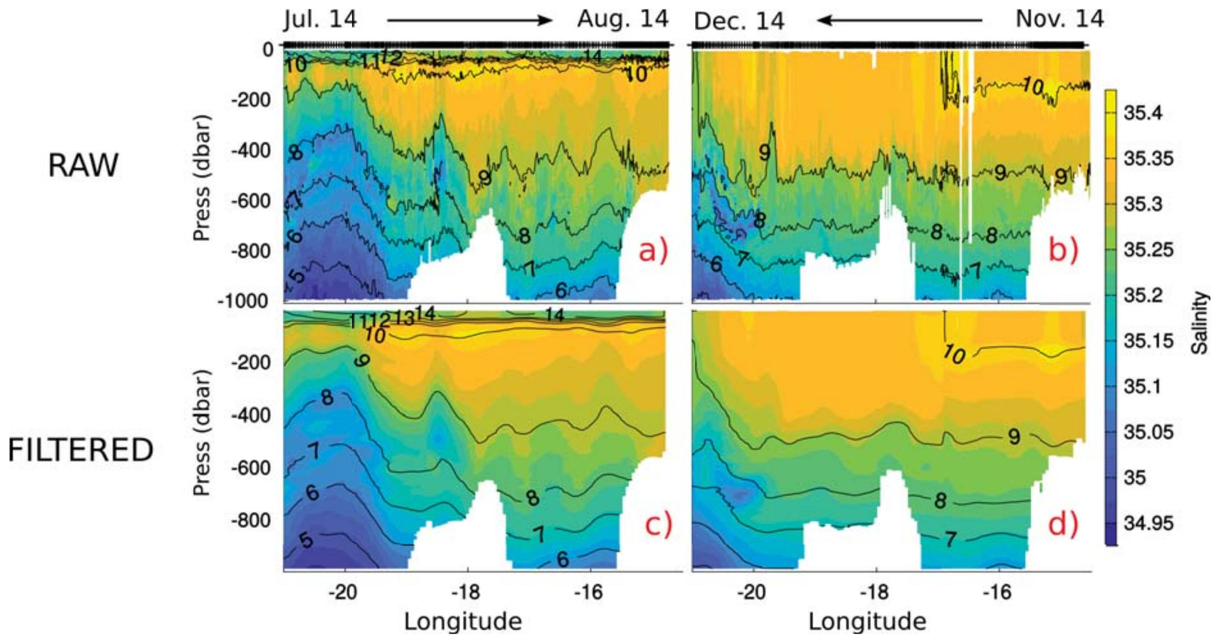

Figure 3. Individual glider sections observed from July to August 2014 (a) and from November to December 2014 (b), showing salinity with potential temperature contour binned in 2m vertical bins; same data filtered using a gaussian moving average of 8km variance corresponding to a full width at half maximum of 18.8km (c, d)

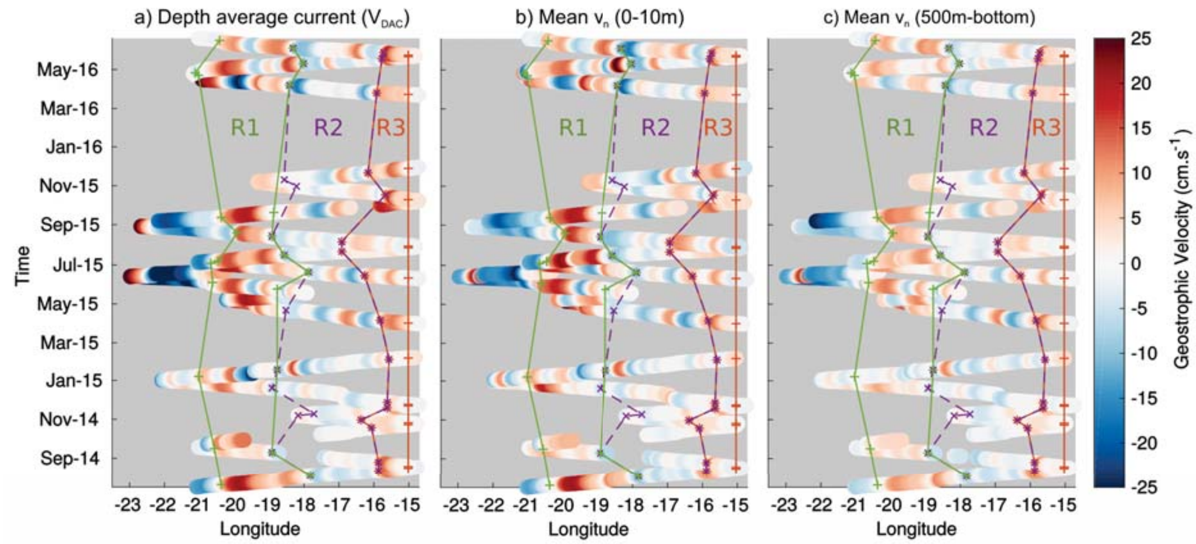

Figure 4. a) Time series of the meridional component of the depth average current, b) time series of the average absolute meridional geostrophic current for the near-surface layer (0-10m) and c) below the seasonal pycnocline (500m-bottom). The western and eastern limits of the three regions mentioned in the manuscript are shown for each section: Region R1 (the Hatton Bank Jet) in green, Region R2 in purple, Region R3 (the Rockall Bank Jet) in red

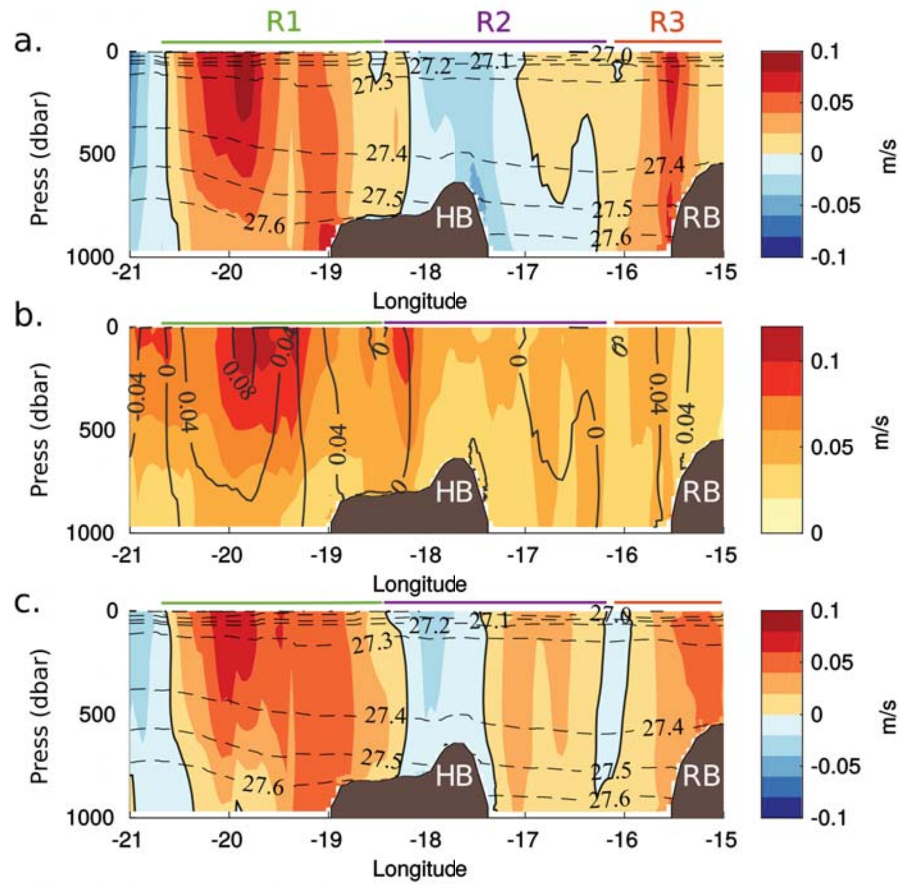

Figure 5. (a) Mean absolute meridional geostrophic velocity (m.s^{-1}) referenced to glider DAC; (b) Standard deviation of the absolute meridional geostophic velocity between glider sections; (c) Mean absolute meridional geostrophic velocity referenced to surface absolute geostrophic current from altimetry; Dashed lines correspond to potential density contours. The solid black contour lines are the 0 m.s^{-1} geostrophic velocity contours.. The mean zonal widths of the three regions R1, R2 and R3 are shown on top of the section (R1: 20.5°W/18.5°W; R2: 18.5°W/16.0°W; R3: 16.0°W/15.0°W).

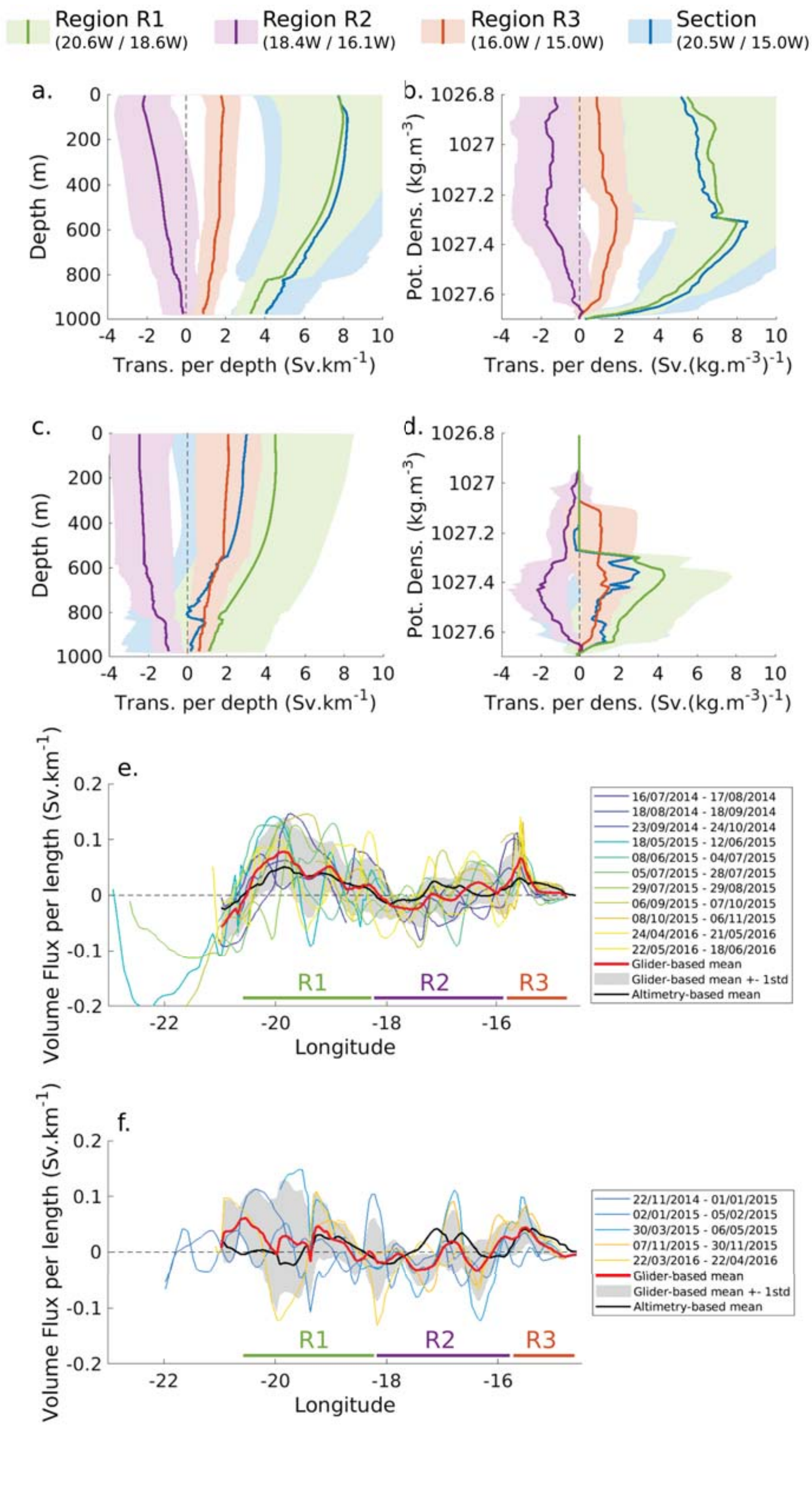

Region R1 (20.6W / 18.6W)
Region R2 (18.4W / 16.1W)
Region R3 (16.0W / 15.0W)
Section (20.5W / 15.0W)
a.
b.
c.
d.
Depth (m)
Pot. Dens. (kg.m-3)
Trans. per depth (Sv.km-1)
Trans. per dens. (Sv.(kg.m-3)-1)
e.
f.
Volume Flux per length (Sv.km-1)
Longitude
R1
R2
R3
16/07/2014 - 17/08/2014
18/08/2014 - 18/09/2014
23/09/2014 - 24/10/2014
18/05/2015 - 12/06/2015
08/06/2015 - 04/07/2015
05/07/2015 - 28/07/2015
29/07/2015 - 29/08/2015
06/09/2015 - 07/10/2015
08/10/2015 - 06/11/2015
24/04/2016 - 21/05/2016
22/05/2016 - 18/06/2016
22/11/2014 - 01/01/2015
02/01/2015 - 05/02/2015
30/03/2015 - 06/05/2015
07/11/2015 - 30/11/2015
22/03/2016 - 22/04/2016
Glider-based mean
Glider-based mean +- 1std
Altimetry-based mean

Figure 6. Mean summer (a,b,e) and winter (c,d,f) absolute meridional geostrophic velocity transport by longitude as a function of depth (a,c), density (b,d) and integrated by depth as a function of longitude (e,f). Shaded areas (on the panels a to d) correspond to the mean transport +/- 1 standard deviation for Region R1 (green), Region R2 (purple), Region R3 (red), and the total section (blue).

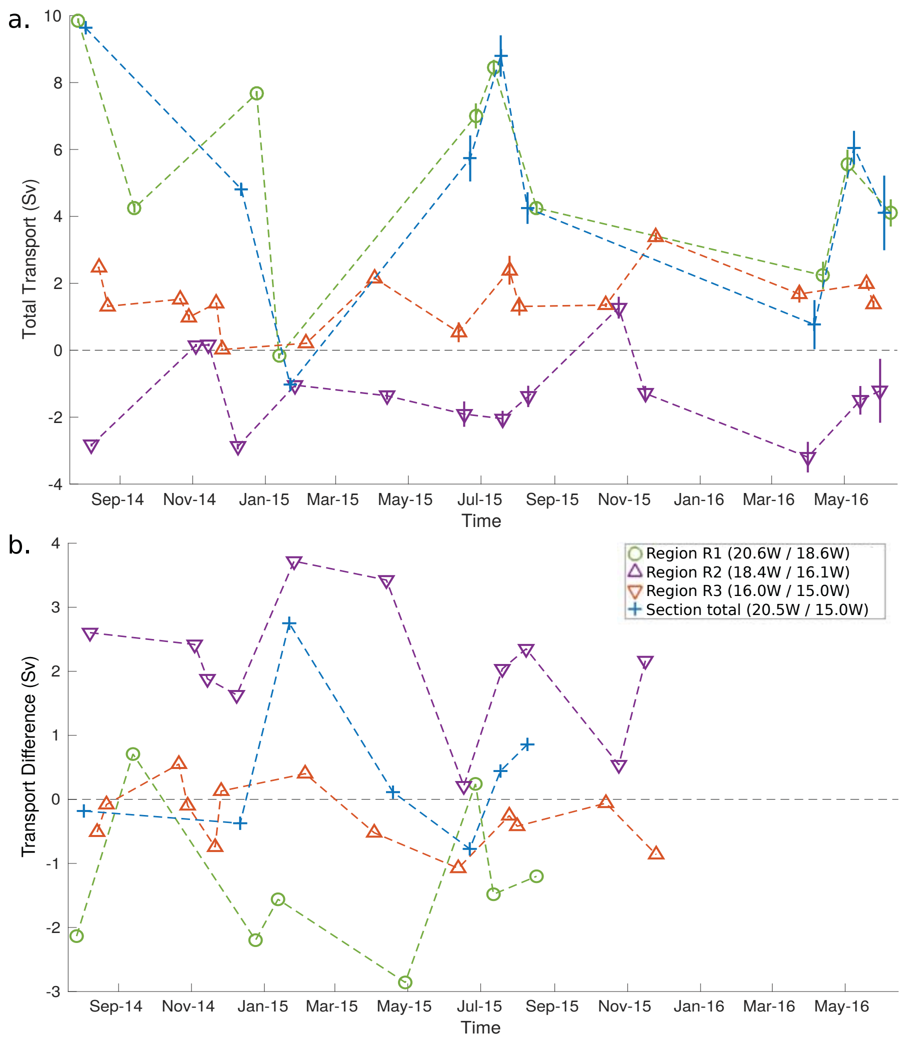

Figure 7. a) Integrated absolute meridional transport for the layer 0-1000m for each glider section along 58° N calculated for regions R1, R2, R3 and the whole section. Uncertainties on individual transport estimated are listed in Table 2 and are indicated by vertical bars. Statistics are summarised in Table 3); b) Time series of the differences between transport calculated with the altimetry-referenced surface geostrophic velocities and glider DAC referenced.

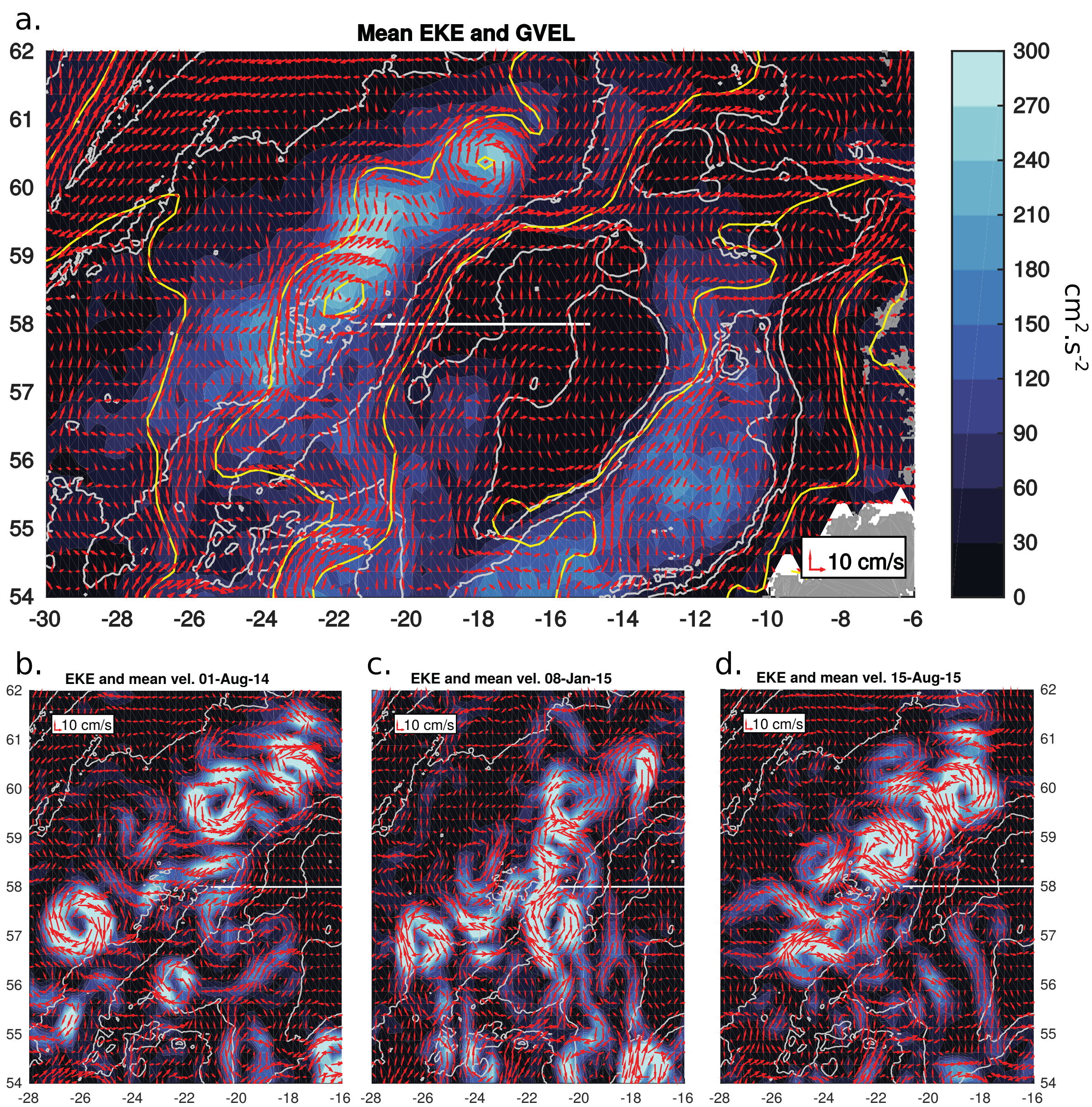

Figure 8. a) Two year mean Eddy Kinetic Energy (blue color scale) and surface Absolute Geostrophic Current (red arrows) for the 2014-2015 period, with mean absolute dynamic topography contours plotted in yellow with a contour interval of 0.1 m (labels shown on Fig. 9), and 1000m-bathymetry contours in grey from GEBCO bathymetry. Daily satellite data are shown for August 1st, 2014 (b), January 8th, 2015 (c) and August 15th, 2015 (d)

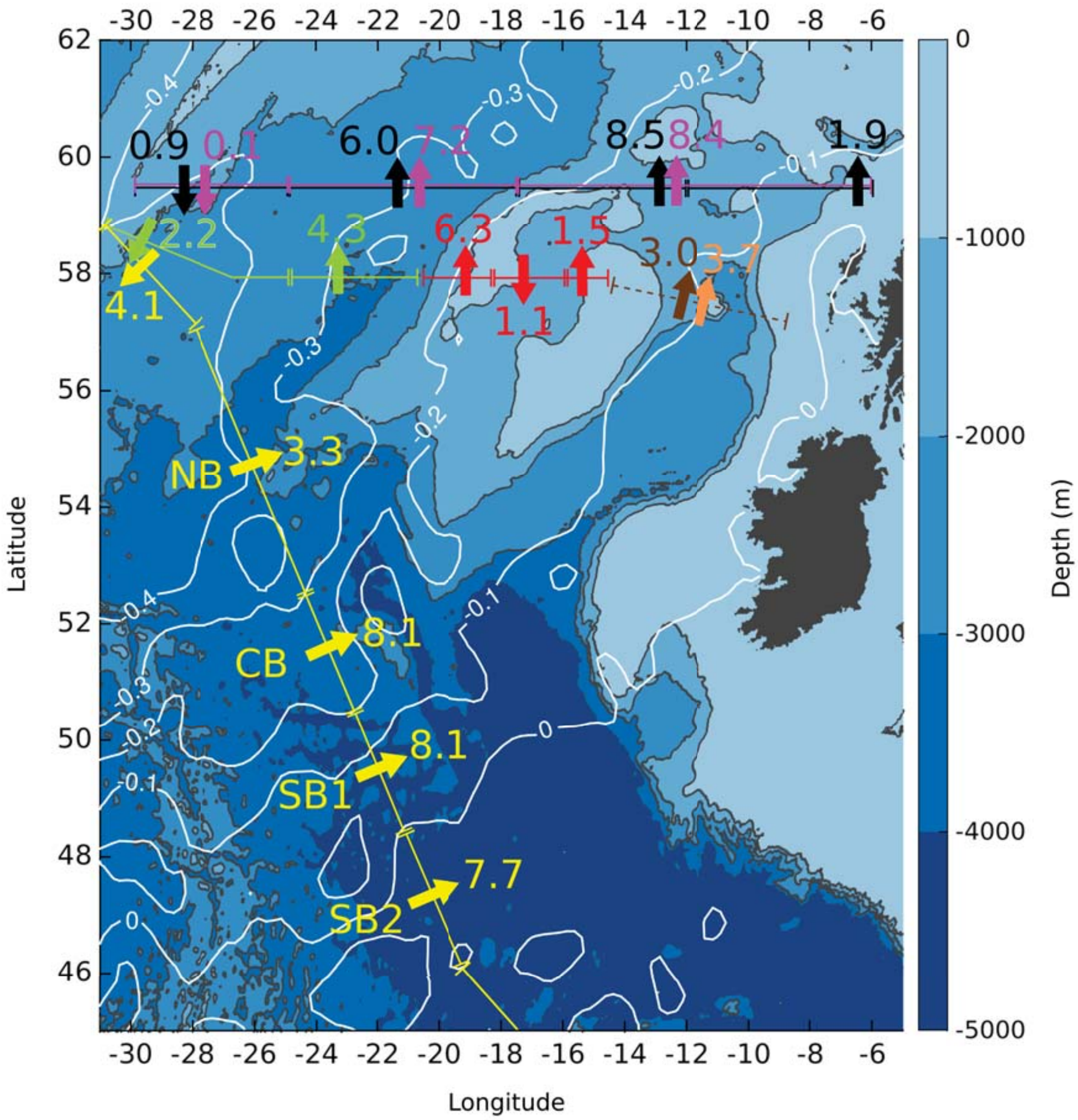

Latitude
Longitude
Depth (m)
NB
3.3
CB
8.1
SB1
8.1
SB2
7.7
4.1
2.2
4.3
6.3
1.1
1.5
3.0
3.7
0.9
0.1
6.0
7.2
8.5
8.4
1.9

Figure 9. Contours in color from GEBCO bathymetry with the upper-ocean transport calculated from various historical and recent observational datasets. The upper-ocean layer is defined as $\sigma_0 < 27.50$ in *Holliday et al.* [2018], $\sigma_0 < 27.55$ in *Sarafanov et al.* [2012] and *Rossby et al.* [2017], $\sigma_1 < 32.15$ in *Daniault et al.* [2016], 1000m in the present study). Each colored arrow is perpendicular to a colored line indicating the length of the section used by the different authors for their transport calculation. The position of each arrow corresponds to the position of the velocity maximum on the section. Transport values are expressed in Sv and are associated with: the 2002-2016 summer mean along the OVIDE section (yellow arrow, see *Daniault et al.* [2016]), the 2002-2008 summer mean from *Sarafanov et al.* [2012] (black arrow along 59.5°N), the 2012-2016 deseasoned mean from *Rossby et al.* [2017] (pink arrow along 59.5°N),the summer mean of the 2014 and 2016 OSNAP hydrographic sections computed by *Holliday et al.* [2018] (light green arrow between 31°W and 21°W), the 2014-2016 summer mean calculated in this study (red arrow along 58°N from 21°W and 15°W). In the Rockall Trough, the northward transport in the upper 1100m relative to a level of no motion ($\sigma_0 = 27.68 kg.m^{-3}$) is indicated as a brown arrow from *Holliday et al.* [2015] who calculated it from 11 complete occupations between 1997 and 2014. For the 1975-1998 period, the northward transport above 1200m, relative to a level of no motion at 1200m, is indicated as a orange arrow (calculated from 24 hydrographic sections, see *Holliday et al.* [2000]). Contours of the mean absolute dynamic topography are plotted in white with a contour interval of 0.1 m. Acronyms: Northern Branch (NB), Central Branch (CB), Southern Branch (SB)

Table 1. Summary of glider mission and sampling on the OSNAP glider endurance line (west of 15°W), including dates, mean and standard deviation of dive displacement and duration, and number of temperature and salinity profiles (dive+climb)

Occupation Dates	Δx (km)	Δt (h)	T profiles	S profiles
16 Jul 2014 to 22 Nov 2014	2.70 ± 1.22	4.33 ± 1.47	658	518
24 Nov 2014 to 21 Feb 2015	2.95 ± 1.65	4.60 ± 1.43	434	432
31 Mar 2015 to 24 Jun 2015	3.58 ± 2.24	5.09 ± 1.08	399	398
10 Jun 2015 to 28 Nov 2015	3.26 ± 1.65	4.93 ± 0.86	804	787
22 Mar 2016 to 22 Jun 2016	3.49 ± 1.64	4.83 ± 0.81	431	431

Table 2. Transport uncertainty (Sv) for each individual glider section (numbered from S1 to S20), defined as 1 standard deviation between the 100 ensemble members of the Monte Carlo approach detailed in Appendix A. The mean uncertainty calculated over all sections and the standard deviation are also indicated.

Section	Region R1	Region R2	Region R3	All
S1	0.07	0.04	0.02	0.11
S2	0.14	N.A.	0.02	N.A.
S3	N.A.	N.A.	0.04	N.A.
S4	N.A.	0.05	0.09	N.A.
S5	N.A.	0.04	0.02	N.A.
S6	0.08	0.08	0.04	0.16
S7	0.05	0.09	0.02	0.12
S8	0.04	0.11	0.04	0.13
S12	0.37	0.38	0.30	0.69
S13	0.24	0.23	0.43	0.62
S14	0.17	0.32	0.27	0.47
S16	N.A.	0.33	0.06	N.A.
S17	N.A.	0.22	0.14	N.A.
S18	0.41	0.45	0.27	0.73
S19	0.43	0.43	0.10	0.50
S20	0.41	0.96	0.10	1.12
Mean	**0.22**	**0.27**	**0.12**	**0.46**
σ	**0.16**	**0.25**	**0.13**	**0.34**

Table 3. Mean ($\overline{x}$), standard deviation (s), standard error (SE), minimum (min), and maximum (max) of the absolute meridional transports (ϕ_{abs}), with the number of available sections (N_{sec}). Positive (negative) transport values are northward (southward).

		ϕ_{abs}					
Period	Area	$\overline{x}$ (Sv)	σ (Sv)	SE (Sv)	min (Sv)	max (Sv)	N_{sec}
All Months	Hatton Bank Jet (20.6°W/18.6°W)	5.1	2.8	0.9	-0.7	9.1	11
	Region R2 (18.4°W/16.1°W)	-1.5	1.3	0.4	-3.4	0.7	14
	Rockall Bank Jet (16.0°W/15.0°W)	1.5	0.9	0.2	0.1	3.3	16
Summer	Hatton Bank Jet (20.6°W/18.6°W)	6.3	2.1	0.8	3.5	9.1	7
	Region R2 (18.4°W/16.1°W)	-1.1	1.4	0.5	-3.4	0.7	7
	Rockall Bank Jet (16.0°W/15.0°W)	1.5	0.7	0.2	0.1	2.4	10
Winter	Hatton Bank Jet (20.6°W/18.6°W)	3.3	3.1	1.6	-0.7	6.4	4
	Region R2 (18.4°W/16.1°W)	-2.0	1.1	0.4	-3.4	-0.7	7
	Rockall Bank Jet (16.0°W/15.0°W)	1.5	1.2	0.5	0.2	3.3	6

Table 4. Same as Table 3 but for the baroclinic transport ϕ_{bc} and the ratio ϕ_{bc}/ϕ_{abs}

			ϕ_{bc}					ϕ_{bc}/ϕ_{abs}				
Period	Area	N_{sec}	μ (Sv)	σ (Sv)	SE (Sv)	min (Sv)	max (Sv)	μ (Sv)	σ (Sv)	SE (Sv)	min (Sv)	max (Sv)
Summer	Hatton Bank Jet	7	2.1	1.3	0.5	0.5	3.9	0.31	0.15	0.06	0.13	0.51
	Region R2	7	-0.2	0.6	0.2	-1.3	0.5	0.11	0.39	0.15	-0.39	0.70
	Rockall Bank Jet	10	0.0	0.3	0.1	-0.4	0.6	-0.04	0.19	0.06	-0.36	0.26
Winter	Hatton Bank Jet	4	2.0	0.6	0.3	1.3	2.8	-0.58	2.08	1.04	-3.69	0.61
	Region R2	7	0.2	0.9	0.3	-0.5	2.0	-0.15	0.58	0.22	-1.36	0.42
	Rockall Bank Jet	6	0.1	0.4	0.1	-0.3	0.7	-0.12	0.65	0.27	-1.37	0.51

Table 5. Same as Table 3 but for the mean and RMS differences in transport derived from glider-based and altimetry-based absolute geostrophic velocity estimates. On each section, differences between absolute geostrophic velocity referenced to glider DAC and referenced to surface absolute geostrophic current from altimetry are calculated for each grid point (every 3km). Then the mean and RMS differences are integrated along the section in order to compare these values to the absolute transport estimated across the section (Table 3).

			$Mean(\phi_{abs}^{glider} - \phi_{abs}^{altimetry})$					$RMS(\phi_{abs}^{glider} - \phi_{abs}^{altimetry})$				
Period	Area	N_{sec}	$\overline{x}$ (Sv)	σ (Sv)	SE (Sv)	min (Sv)	max (Sv)	$\overline{x}$ (Sv)	s (Sv)	SE (Sv)	min (Sv)	max (Sv)
All Months	Hatton Bank Jet	8	-1.3	1.2	0.4	-2.9	0.7	6.3	2.9	1.0	1.8	9.6
	Region R2	11	2.1	1.1	0.3	0.2	3.7	5.8	2.7	0.8	2.7	10.6
	Rockall Bank Jet	13	-0.3	0.5	0.1	-1.1	0.6	1.7	0.6	0.2	0.8	2.6
Summer	Hatton Bank Jet	5	-0.8	1.2	0.5	-2.1	0.7	4.8	2.6	1.2	1.8	8.8
	Region R2	5	1.6	1.1	0.5	0.2	2.6	4.7	2.3	1.0	2.7	8.5
	Rockall Bank Jet	8	-0.2	0.5	0.2	-1.0	0.6	1.9	0.6	0.2	1.2	2.6
Winter	Hatton Bank Jet	3	-2.2	0.7	0.4	-2.9	-1.6	8.8	0.8	0.5	7.9	9.6
	Region R2	6	2.5	0.9	0.4	1.6	3.7	7.0	2.8	1.2	3.7	10.6
	Rockall Bank Jet	5	-0.3	0.6	0.3	-0.9	0.4	1.4	0.7	0.3	0.8	2.4

Table 6. Summary of the true heading errors for the different glider mission determined by all available on-land compass calibration checks carried out before or after the deployment. For four of the five glider deployments, the compass calibration was checked in land [GROOM, 2014], before or after the glider mission. The terms Err_{port} and Err_{stbd} indicate the heading error from compass checks made with different orientations of the glider (turned on port and starboard). For OSNAP3 and OSNAP4, the compass checks for different orientations of the glider was not possible. An Err_{min} and Err_{max} variable is defined for OSNAP3 by using the single-orientation compass check and by adding the maximal difference recorded between a compass check with a starboard orientation and a port orientation (8°). No on-land compass check was available for the OSNAP4 glider mission due to the lost of the glider at the end of the mission. However an in-flight compass calibration was performed at beginning of the mission, thus we determined the heading error as the maximal post-mission heading error recorded for a glider which performed an in-flight compass calibration (6°).

	OSNAP1		OSNAP2		OSNAP3		OSNAP4		OSNAP5	
Abs. Bearing	Err_{port}	Err_{stbd}	Err_{port}	Err_{stbd}	Err_{min}	Err_{max}	Err_{min}	Err_{max}	Err_{port}	Err_{stbd}
30	-0.5	4.0	-13.5	-14.0	-5.0	3.0	-6.0	6.0	-1.5	5.7
60	1.5	4.0	-10.0	-9.0	0	8.0	-6.0	6.0	4.0	7.0
90	3.5	4.0	-3.5	-2.0	-2.0	6.0	-6.0	6.0	7.5	6.0
120	-1.5	-2.0	0.5	2.0	-5.5	2.5	-6.0	6.0	7.5	2.5
150	2.5	0	12.0	14.0	-3.5	4.5	-6.0	6.0	7.0	0
180	-3.0	-6.0	10.5	11.5	-7.0	1.0	-6.0	6.0	4.0	-3.0
210	-1.5	-5.4	4.5	4.5	-11.5	-3.5	-6.0	6.0	2.0	-5.0
240	-1.5	-2.0	2.5	1.0	-11.5	-3.5	-6.0	6.0	-2.0	-5.0
270	-3.5	-4.0	0.5	-1.0	-13.0	-5.0	-6.0	6.0	-4.0	-4.0
300	-2.0	1.0	-2.5	-4.5	-7.0	1.0	-6.0	6.0	-7.0	-3.0
330	-2.0	2.0	-5.0	-6.5	-6.5	1.5	-6.0	6.0	-7.0	0.5
360	-0.5	4.0	-7.0	-7.5	-1.5	6.5	-6.0	6.0	-5.0	4.0
In water calib.	X						X		X	
Pre-mission check					X				X	
Post-mission check	X		X				X			